UNIVERSITÀ DEGLI STUDI DI GENOVA

Scuola di Scienze Mediche e Farmaceutiche

Dottorato di Ricerca XXXVIII CICLO

EMATO ONCOLOGIA E MEDICINA INTERNA CLINICO-TRASLAZIONALE

Orientamento:

ONCOLOGIA TRASLAZIONALE

Coordinatore: Prof. Alessio Nencioni

Myxofibrosarcoma characterization to generate novel preclinical models and test tailored therapies

Relatrice:
Prof.ssa Lucia Del Mastro

Co-relatrice:
Dott.ssa Michela Croce

Candidato:
Dott. Massimiliano Grassi

INTRODUCTION

Myxofibrosarcoma

Soft tissue sarcomas (STS) are a heterogeneous group of rare malignancies of mesenchymal origin, with an estimated incidence of approximately 4–5 cases per 100,000 persons per year in Western countries [1]. In Europe, data from the RARECARE project have confirmed the rarity of these tumors, highlighting substantial heterogeneity in terms of age distribution, anatomical site, and histological subtype [2]. STS comprise more than 70 distinct histological subtypes, characterized by different biological behaviors and therapeutic responses [1].

Within this group, myxofibrosarcoma (MFS) and undifferentiated pleomorphic sarcoma (UPS) represent biologically and clinically related entities, sharing high genomic heterogeneity and an aggressive clinical behavior [3]. Histologically, MFS is characterized by a myxoid stroma, pleomorphic neoplastic cells, and a distinctive infiltrative growth pattern along fascial planes. Historically included within the spectrum of malignant fibrous histiocytoma, MFS has been progressively recognized as a distinct entity in the WHO classifications of soft tissue tumors [1,4].

From an epidemiological standpoint, MFS accounts for a minority of STS cases but is relatively frequent in the elderly population, with a peak incidence between the sixth and eighth decades of life and a slight male predominance [4,5]. The most common primary site is the extremities, particularly the lower limbs. Clinically, MFS often present as a slowly growing, minimally symptomatic mass [4,5].

A hallmark feature of MFS is its marked propensity for local recurrence, which is attributed to microscopic infiltrative growth that extends beyond the macroscopically apparent tumor margins [5]. Radiologic–pathologic studies have demonstrated that this subclinical extension correlates with specific magnetic resonance imaging findings, such as the so-called “tail sign” [6,7]. Histologically, MFS displays a broad morphological spectrum, ranging from low-grade to high-grade lesions. Typical features include a multinodular growth pattern, abundant myxoid extracellular matrix, elongated curvilinear blood vessels, and spindle-shaped or stellate tumor cells with variable degrees of nuclear atypia [5].

Low-grade MFS is characterized by low cellularity and mild cytological atypia. In contrast, intermediate- and high-grade tumors demonstrate progressively increased cellular density, marked pleomorphism, brisk mitotic activity, and areas of tumor necrosis [5]. High-grade MFS may closely resemble UPS, making the identification of residual myxoid stroma a key element for differential diagnosis [3,5].

Several histopathological parameters have been shown to carry prognostic significance. A higher proportion of myxoid stroma has been associated with more favorable outcomes, whereas increased

angiogenesis and higher microvessel density correlate with an elevated risk of metastatic spread and poorer prognosis [5].

The management of patients with locally advanced MFS should be centralized in referral sarcoma centers and conducted within a dedicated multidisciplinary team [8]. Appropriate preoperative assessment includes magnetic resonance imaging of the primary tumor site and chest computed tomography for distant staging [9].

Surgery represents the cornerstone of treatment for localized and locally advanced disease [10]. In MFS, the goal is to achieve a complete resection with microscopically negative margins (R0), which often requires a wide surgical approach because of the tumor's propensity for microscopic spread beyond apparent boundaries [11]. Adequate local control has been shown to directly impact overall survival in patients with extremity STS [12,13].

Radiotherapy plays a key role in improving local control in patients at high risk of recurrence [11,14]. It may be delivered in the neoadjuvant or adjuvant setting according to established principles for extremity STS [14].

The role of chemotherapy in locally advanced MFS remains selective. Disease-specific studies have demonstrated activity of anthracycline- and ifosfamide-based regimens in advanced MFS [15]. In addition, randomized trials in high-risk STS populations support the use of neoadjuvant chemotherapy in selected cases [16]. More recently, a randomized clinical trial showed a benefit from the addition of pembrolizumab to radiotherapy and surgery in the neoadjuvant setting of high-risk extremity STS [17,18].

The management of metastatic MFS generally follows principles established for advanced STS [9]. Doxorubicin-based chemotherapy remains the standard first-line treatment, with the possible addition of ifosfamide in patients with good performance status [19].

After failure of first-line therapy, pazopanib represents a treatment option for patients with pretreated non-adipocytic STS [20].

In recent years, immunotherapy has generated increasing interest in the treatment of MFS. Translational studies have demonstrated that the MFS tumor microenvironment is immunologically active, providing a biological rationale for the use of PD-1/PD-L1 inhibitors [17]. Phase II clinical studies have shown some activity of immunotherapy in selected STS subgroups [21,22].

Genetic alterations in myxofibrosarcoma: the central role of TP53

MFS is one of the STS characterized by the highest degree of genomic instability. Its molecular landscape comprises a complex combination of single-nucleotide variants (SNVs), copy number alterations (CNAs), and profound structural chromosomal abnormalities [8]. Histological progression of MFS is associated with a progressive increase in cytogenetic alterations, supporting a multistep model of tumor evolution; accordingly, triploid and tetraploid chromosomal profiles are frequently observed in high-grade lesions [23].

Comparative genomic hybridization (CGH) studies have identified recurrent patterns of chromosomal gains and losses in MFS, including gains of 19p and 19q, losses of 1q, 2q, 3p, 4q, 10q, 11q, and 13q, as well as high-level amplifications involving chromosome 1, 5p, and 20q [24]. Additional analyses documented gains of 7p21–22, 7q21–22, 7q31–35, 9q22, 12p13-pter, 12q15–21, 17q22–23, and the X chromosome, together with losses affecting, among others, regions 7p12, 10p13–14, 11p11–14, 13q14–34, and 21q22 [8,25]. In this context, polysomy of chromosome 7 has been associated with MET overexpression, which correlates with deep tumor location, higher histological grade, and more advanced disease stage [6,26]. More recent molecular profiling studies have confirmed activation of the HGF/MET signaling axis in a subset of MFS cases [27].

Although the overall mutational burden of MFS is relatively low compared with other solid tumors, targeted analyses have revealed a high frequency of TP53 alterations. Using a cancer hotspot mutation panel, Heitzer et al. identified TP53 mutations in 44% of cases, whereas variants in other genes, such as *CDKN1A*, *FGFR3*, *PTEN*, and *RB1*, were rare (approximately 1%) [28]. In the same study, low-coverage whole-genome sequencing confirmed the presence of numerous CNAs affecting known cancer driver genes, including *TP53*, *RB1*, and *CDKN2A*, and further demonstrated increased genomic complexity in high-grade tumor areas compared with low-grade regions within the same tumor [28].

The central importance of TP53 in MFS has been further corroborated by whole-exome sequencing (WES) studies. In a cohort of 41 paired tumor–normal samples, 127 recurrently mutated genes were identified; however, TP53 was the only gene significantly associated with MFS [29]. In this study, TP53 mutations were detected in 22% of cases, followed by alterations in *NTRK1* and *NF1* (7% each), as well as in genes not previously linked to MFS, such as *ATRX* (10%) and *TET2* (7%) [2915]. When SNVs, CNAs, and gene fusions were considered jointly, TP53 emerged as the most frequently altered gene, together with key regulators of the G1/S cell cycle transition, including *CDKN2A*, *CDKN2B*, *CCND1*, and *RB1* [29].

A subsequent expanded analysis of 116 cases confirmed the presence of driver alterations in TP53 in 46% of MFS, followed by alterations in *RB1* (18%), *CDKN2A* (16%), *CDKN2B* (16%), *NF1* (11%),

and *NTRK1* (9%), reinforcing the hypothesis that dysregulation of the p53 pathway and cell cycle control represents a cornerstone event in MFS development [29].

By integrating their findings with TCGA datasets, Takeuchi et al. analyzed a total of 102 MFS samples, confirming a high frequency of alterations in *TP53* (24.5%), *RB1* (22.5%), *ATRX* (14.7%), and *NF1* (8.9%), along with the identification of several novel candidate driver genes [19]. Beyond the well-characterized focal amplifications and copy number losses, recurrent alterations were detected in genes involved in structural and transcriptional regulation, suggesting additional layers of genomic complexity in MFS [30].

More recently, an integrated immunohistochemical and genetic analysis of primary MFS cases demonstrated that high-grade tumors are significantly associated with MET positivity and, importantly, that the combined presence of TP53 SNVs and CNAs represents an independent risk factor for poorer 5-year event-free survival [31]. In this series, TP53 alterations were identified in 86.4% of cases, underscoring the dominant role of p53 in driving the biological aggressiveness of MFS [31].

Beyond its classical cell-autonomous functions—including cell cycle arrest, apoptosis, senescence, and regulation of the DNA damage response—p53 also plays a fundamental role in modulating the tumor microenvironment (TME). Specifically, p53 inhibits angiogenesis, limits the activity of regulatory T cells and myeloid-derived suppressor cells, promotes the expression of major histocompatibility complex class I molecules, enhances the secretion of pro-inflammatory cytokines, and downregulates PD-L1 expression, thereby facilitating cytotoxic T lymphocyte and natural killer cell activity [32,33]. In addition, p53 contributes to macrophage polarization toward an antitumoral M1 phenotype [32,33].

In MFS, however, the relationship between TP53 status and immunological features of the TME remains poorly defined. Chen et al., analyzing a cohort of 254 sarcoma patients, including 25 cases of MFS, found no significant correlation between TP53 mutations and global immune scores [34]. This finding may reflect methodological limitations, as TP53 mutations are highly heterogeneous from a functional standpoint and may result in loss of function, dominant-negative effects, or gain-of-function oncogenic activities [35].

Considering these observations, a more comprehensive functional characterization of the p53 alteration landscape in MFS, integrated with detailed analysis of the tumor microenvironment, may provide novel insights into disease progression and therapeutic response. Indeed, studies in other solid tumors have demonstrated that specific TP53 mutational patterns are associated with distinct prognostic outcomes and immune infiltration profiles [36,37]. Therefore, TP53 emerges as a potential prognostic biomarker and a promising therapeutic target in myxofibrosarcoma, further emphasizing the value of molecular profiling in this highly complex malignancy.

The Extracellular Matrix in Myxofibrosarcoma

Among myxoid soft tissue tumors, myxofibrosarcoma (MFS) displays a distinctive stromal architecture that is central to its histopathological identity and biological behavior. The myxoid extracellular matrix (ECM) is a dynamic and bioactive compartment that actively regulates tumor proliferation, migration, invasion, and interactions with surrounding tissues.

MFS is characterized by an ECM enriched in glycosaminoglycans (GAGs), proteoglycans, and associated signaling molecules. Hyaluronic acid (HA) is the predominant GAG, accompanied by sulfated GAGs such as chondroitin and keratan sulfate, accounting for the gelatinous appearance of the tumor [38,39]. Proteoglycans including versican, aggrecan, and decorin interact with HA to form large hydrated aggregates that regulate ECM organization, growth factor availability, and tissue mechanics. Variability in ECM composition among tumors may contribute to differences in clinical behavior and recurrence risk [39].

HA accumulation generates a highly hydrated, gel-like matrix that increases interstitial fluid pressure and solid stress, leading to vascular compression, reduced perfusion, hypoxia, and impaired drug delivery. These biomechanical effects promote resistance to chemotherapy and radiotherapy [40,41]. Beyond its physical properties, HA actively signals through receptors such as CD44 and RHAMM, activating pathways involved in proliferation, migration, epithelial-to-mesenchymal transition, inflammation, and resistance to apoptosis [41].

In MFS, abundant HA contributes to the characteristic hypocellularity and wide interstitial spaces, facilitating infiltrative growth along fascial planes [38]. HA is dynamically remodeled through regulated synthesis and degradation, and its biological effects depend on molecular weight: high-molecular-weight HA mainly provides structural support, whereas fragmented HA promotes pro-tumorigenic signaling and invasion [42,43].

The HA–CD44 axis represents a major signaling hub in MFS, activating pathways such as Ras–MAPK, PI3K–AKT, and Src, and correlating with local recurrence and poor prognosis [44,45]. HA also interacts with RHAMM to promote focal adhesion signaling and directional migration, mechanisms well documented in fibrosarcoma and likely relevant to MFS [42,46].

Although HA dominates the myxoid matrix, fibrillar collagens, particularly types I and III, are variably present and tend to increase with tumor grade. These fibers remain loosely organized within the hydrated ECM, preserving permissiveness to cell migration, while basement membrane components are sparse or discontinuous, consistent with infiltrative behavior [38–40,47].

Overall, the ECM of MFS exemplifies dynamic reciprocity between tumor cells and stroma, with reciprocal regulation of signaling, matrix composition, and growth factor availability [48]. From a clinical perspective, qualitative features of the ECM—such as HA turnover, receptor expression, and molecular weight distribution—may better predict tumor behavior than ECM abundance alone.

Targeting HA metabolism or HA-receptor interactions therefore represents a promising therapeutic avenue in MFS [39,45].

Myxofibrosarcoma tumor microenvironment

The TME of MFS plays a critical role in tumor progression and response to immunotherapy through complex interactions between malignant cells and immune components, including dendritic cells, tumor-infiltrating lymphocytes, and macrophages [49].

Although a comprehensive characterization of the MFS TME is still lacking, recent studies have revealed marked heterogeneity in immune infiltration patterns, enabling the identification of distinct immunological subtypes with prognostic and predictive relevance. Integrated clinical and genomic analyses have classified MFS samples into three immune clusters: i) predominant infiltration of $CD4^+$ T cells, activated NK cells, monocytes, and M2 macrophages; ii) enrichment of B cells, resting NK cells, and M0 macrophages; iii) an immune-inflamed TME with high levels of $CD8^+$ T cells, follicular helper T cells, γδ T cells, and M1 macrophages. Cluster iii) was associated with increased sensitivity to immunotherapy [50].

Dendritic cells are professional antigen-presenting cells that initiate and regulate adaptive immune responses by activating T lymphocytes [51]. Within the MFS microenvironment, dendritic cells—often present in an immature state—appear to contribute to antigen presentation and have been associated with improved disease-free survival, irrespective of tumor grade [52].

Tumor-infiltrating lymphocytes encompass both effector and immunosuppressive populations. Infiltrating T cells, expressing immune checkpoint molecules such as TIM-3 and LAG-3, have been identified in a significant proportion of MFS cases, hypothesizing a role for these molecules in immune evasion and T-cell exhaustion; this is a dynamic process driven by chronic antigen stimulation and sustained inflammatory signaling, resulting in impaired cytotoxic function and reduced proliferative capacity [22,49].

Regulatory T cells (Tregs), by suppressing effector T-cell responses and promoting tumor immune tolerance, have been linked to an increased risk of local recurrence, suggesting a key role in immune evasion mechanisms [53,54].

Tregs exert immunosuppressive effects through checkpoint molecule expression, including CTLA-4, PD-1, and LAG-3, downregulation of costimulatory molecules on dendritic cells, and secretion of immunosuppressive cytokines such as TGF-β, which further enhances Treg function and inhibits antigen-presenting cell activation [55,56].

Consistently, high expression of immune checkpoint molecules, including PD-1, PD-L1, TIM-3, and LAG-3, has been reported in a substantial proportion of MFS cases, indicating a strongly immunoregulatory TME that may nonetheless be amenable to immune checkpoint blockade [57–61].

The presence of pre-existing $CD8^+$ T cells and PD-1^+ T cells within the TME has been associated with improved responses to PD-1 inhibitors such as pembrolizumab [22,61–63].

Finally, tumor-associated macrophages constitute a major component of the MFS TME, with a predominance of M2-like, anti-inflammatory phenotypes that promote immunosuppression and tumor progression, while computational analyses suggest enrichment of immunosuppressive myeloid populations, including putative myeloid-derived suppressor cells, although direct studies in MFS remain lacking [50,59,61,64].

Overall, the MFS TME is characterized by a highly immunosuppressive milieu, supporting the rationale for combinatorial therapeutic strategies targeting Tregs, M2 macrophages, and other suppressive immune components to enhance immunotherapy efficacy in this disease.

AIM OF THE STUDY

MFS represents a paradigmatic example of the challenges of sarcoma research, as it combines pronounced biological heterogeneity, the absence of defining genetic drivers, limited experimental models, and a strong dependence on the TME. Studies on MFS are further constrained by the small number of patients, reflecting the rarity of the disease, and by the advanced age of affected individuals, who are frequently ineligible for surgery due to health-related exclusions. In this context, a deeper characterization of the immunological features of MFS, together with the development of robust preclinical models in which different therapeutic strategies can be evaluated, is critically needed to improve biological understanding and guide the design of more effective treatments. Although MFS lacks recurrent targetable oncogenic alterations, TP53 is frequently altered and has been linked to tumor progression and genomic instability, yet its functional impact remains poorly understood. In the present project, we performed an in-depth characterization of patient-derived specimens, focusing on the TME, T cell exhaustion, and immunosuppressive populations, and investigated the functional consequences of TP53 alterations. We also developed representative 2D and 3D patient-derived models, characterized primary cell lines, and evaluated their response to pharmacological agents. Collectively, this work establishes a platform of preclinical MFS models to support the rational development of biology-driven therapeutic strategies, including drug combinations.

MATERIALS AND METHODS

Patients' enrollment and sample collection

Surgical interventions and sample collections were performed at IRCCS Ospedale Policlinico San Martino by the sarcoma surgery and/or radiology team. All diagnoses were reviewed and confirmed by an expert sarcoma pathology of our hospital. Targeted RNA sequencing using the FUSIONPlex™ Sarcoma v2 Panel (ArcherDx) identified sarcoma-associated gene fusions involving: ALK, BCOR, BRAF, CAMTA1, CCNB3, CIC, CSF1, CTNNB1, EGFR, EPC1, ERG, ESR1, ETV1, ETV4, ETV5, ETV6, EWSR1, FGFR1, FGFR2, FGFR3, FOS, FOSB, FOXO1, FUS, GLI1, HMGA2, JAZF1, MBTD1, MDM2, MEAF6, MET, MGEA5, MKL2, MYOD1, NCOA1, NCOA2, NCOA3, NR4A3, NTRK1, NTRK2, NTRK3, NUTM1, PAX3, PDGFB, PDGFRA, PHF1, PLAG1, PRKCA, PRKCB, PRKCD, RAF1, RET, ROS1, SS18, STAT6, TAF15, TCF12, TFE3, TFG, USP6, VGLL2, YAP1, YWHAE), and was applied to all patient-derived samples.

Primary cell line development

Surgical samples were minced with a scalpel to obtain 2x3mm fragments; some fragments were frozen for future experiments, while the rest were incubated stirring for 3 hrs with 5 mg/ml Collagenase I (Sigma) in HBSS (Gibco) at 37°C to digest matrix and free tumor and immune cells. After matrix digestion, cells were washed with complete Dulbecco's modified Eagle's medium (DMEM), isolated from the aggregates using 100-µm sterile filters (Corning, Merck Life Science srl, Milan, Italy) and seeded in standard monolayer cultures. MFS cells grow quite slowly in the first passages, but growth speeds up after some divisions. Cells were frozen at every passage. After the 10^{th} passage, we consider the cells spontaneously immortalized.

To increase the number of primary cell lines, two additional cell lines (S148 and S11) were kindly provided by our collaborator Dr. A. De Vita (IRCCS Istituto Romagnolo Per Lo Studio Dei Tumori (IRST) "Dino Amadori").

All MFS cell lines grow in a complete DMEM medium (10% FBS, 1% Pen/Strep, 2% glutamine, 1% HEPES, and 1% NEAA) at 37°C in a 5% CO2 atmosphere.

Cell treatment and flow cytometry analysis

Primary MFS cell lines were harvested, washed with PBS1x, and stained with fluorescently labeled antibodies against HLA-class I (W6.32), HLA-class II (D1.12), CD105, FAP, and PD-L1 (BD Biosciences). Human interferon-gamma (IFN-γ, 100 ng/mL) was administered for 72 h to MFS cell lines to induce HLA-class I, -class II, and PD-L1 expression. Surface expression was analyzed by

flow cytometry (BD Symphony A3), and data were processed using FlowJo v10. Untreated cells served as controls.

Drug testing

Doxorubicin hydrochloride (Sigma-Aldrich, Saint Lous, MO, USA) was dissolved in water at a concentration of 25 mM, and stored in aliquots at -80°c. Palifosfamide (MedChemExpress, Sollentuna, Sweden), was dissolved in DMSO at a concentration of 180.98 mM, and stored in aliquots at -80°c.

Primary cell lines (7000 cells/well) were seeded in 96-well plates, and the next day treated with different concentrations of palifosfamide (100 mM-1mM) or doxorubicin (0.5-100 mM). Cell proliferation was assessed by CellTiter 96® AQueous One Solution (Promega) following manufacturer instructions after 72 hours and 7 days. IC_{50} (Half Maximal Inhibitory Concentration), the concentration of a drug at which the response or activity is reduced by 50% compared to a control without the drug, was assessed after 7days treatment, using Prism 9.4 (GraphPad Software, San Diego, CA, USA).

Western Blot

Primary cell lines (500000 cells in a T25 flask) were irradiated (10 Gy; IBL 437 C irradiator (CIS Bio International, Saclay, France)) to generate DNA damage, which is one of the strongest and most reproducible stimuli for the p53 pathway. After irradiation, flasks were kept in an incubator, and cells were lysated after 2, 4, and 8 hours of culture. Total proteins were extracted using cOmplete Lysis-M buffer (Roche, Mannheim, Germany) containing protease inhibitors (Roche) and phosphatase inhibitors (Roche) from untreated and irradiated cell lines. Protein lysates were separated by NuPage 4–12% Bis-Tris Gel (Invitrogen) under reducing conditions. Western blotting was performed according to standard techniques, rabbit anti-p53 (DO-1) (Santa Cruz Biotechnology, Dallas, TX, USA), mouse anti-p21 (Abcam, Cambridge, UK), rabbit anti-mouse/human β-tubulin-HRP (Abcam), and secondary antibody anti-rabbit-HRP (Agilent) and anti-mouse-HRP (Dako Denmark, Glostrup, Denmark). Immunoreactive proteins were detected by ECL Prime (GE Healthcare) and a chemiluminescence gel documentation and analysis system (MINI HD, UVITEC, Cambridge, UK). Densitometric analysis was performed by calculating the ratio of the volume occupied by TP53 or p21 to that of the β-tubulin housekeeping band.

RNA extraction, PCR analysis, and Functional Assay of Separated Alleles in Yeast

RNA was extracted from the cells' pellets (RNeasy Kit Qiagen). cDNA synthesis was performed starting from 0.5 ug of RNA (Biotechrabbit cDNA synthesis kit). The following primers were used

for PCR amplification of human P53 coding sequence (Pfu Polymerase, Biotechrabbit; template cDNA 25ng/ul: 25 ng; annealing primers 55°C, 30 cycles): P3 (forward 5'-ATTTGATGCTGTCCCCGGACGATATTGAAC) and P4 (reverse 5'-CCTTTTTGGACTTCAGGTGGCTGGAGTG-3') (nt 125-1122> codon 42-374: 1000 bp fragment) or P53_ATG forward (5'-ATGGAGGAGCCGCAGTCAGATCCTAGCGTC) and P53_STOP reverse (5'-TCAGTCTGAGTCAGGCCCTTCTGTCTTGAA-3') (nt 1-1179> codon 1-393: 1200 bp fragment)**.**

The Functional Assay of Separated Alleles in Yeast (FASAY) technique is used to study the TP53 functional status. The assay exploits homologous recombination between the terminal ends of i) a PCR product (e.g., P53 human coding sequence) and ii) a yeast expression vector that is specifically digested; then, in yeast a plasmid expressing the P53 coding sequence is reconstituted. The haploid *S. cerevisiae* yIG397 strain (MATa ade2-1 leu2-3,112 trp1-1 his3-11,15 can1-100, ura3-1 URA3 3xRGC::pCYC1::ADE2) is exploited to define the P53 function status. For our analysis, we used the pRDI22 plasmid (LEU2, leucine selection, and ADH1 constitutive expression of P53) that lacks the central sequence coding for the entire p53 DNA-binding domain (Ishioka et al., 1993); the plasmid (1-2 ug) was digested with HindIII-StuI restriction enzymes (New England Biolabs, NEB). The HindIII-StuI–digested pRDI22 plasmid also contains two regions homologous to the terminal regions of the P53 PCR products obtained using P3 and P4 primers. After co-transfection of unpurified PCR products (5 ul) and HindIII-StuI–digested pRDI22 (50 ng) in yIG397, a p53 expression vector having the promoter region derived from pRDI-22 (ADH1) and the core region of the p53 open reading frame derived from P3/P4 PCR product of cell lines (codon 42-374), was reconstituted. When cells express a P53 (i.e., wild type) that functions as a transcription factor in yeast, the ADE2 gene is expressed with consequent formation of white normal-sized colonies; conversely, cells containing a mutant P53 protein grow as small red colonies due to the accumulation of a colored intermediate in the adenine biosynthetic pathway. The functional status of TP53 gene is therefore defined by the percentage of red colonies over the total number of white and red colonies. The colonies were counted after 3 days of growth at 30°C. When analyzing the TP53 status of a cell line, the presence of a wild-type P53 is expected to generate 85-100% white colonies, while the presence of a not functional TP53 mutation at a heterozygous state results in approximately 50% small red colonies; conversely, the presence of homozygous TP53 mutation (s) results in 100% small red colonies.

Sanger sequencing for TP53

Purified PCR products (PCR purification kit, Qiagen) were checked by Sanger sequencing (BMR Genomics, Padova) using two internal primers P5 (forward 5'-TggCCATCTACAAgCAgTCA-3', nt 479> codon 160), and P6 reverse 5'-gggCACCACCACACTATgTC-3', nt 638>codon 213).

Tridimensional (3D) growth of primary MFS cells

Collagen-based scaffolds, gently donated by IRCCS Istituto Romagnolo Per Lo Studio Dei Tumori (IRST) "Dino Amadori", were sterilized by incubating with 70% ethanol for 25 minutes, at room temperature, then washed with sterile PBS1x or media for 10 minutes, twice. PBS was aspirated thoroughly to minimize residual liquid, and scaffolds were left under the biosafety cabinet to air-dry. They were then transferred to agarose-coated 6-well plates (1%) to prevent cell diffusion and adhesion to the well surface. Approximately 2 x 10^6 cells were seeded per scaffold in a minimal volume of medium (10–15 µL) to reduce cell loss by diffusion. After 1–2 hours in the incubator, 5 mL of complete medium is added, and cells are cultured for up to 7 days, depending on the cell line and experiment. The scaffolds were collected and formalin-fixed paraffin-embedded for pathological assessment. Hematoxylin and eosin staining to assess cellular morphology, nuclear atypia, and extracellular matrix deposition.

Multicolor Flow Cytometry Characterization of the Myxofibrosarcoma Tumor Microenvironment

Minced fragments were placed into the GentleMACS C tube in RPMI 1640 medium complete containing enzyme H and A (Miltenyi biotech), put on GentleMACS Octo Dissociator with Heaters, using 37C_h_TDK_3 program. After one hour of incubation, the tube was retrieved, and its contents were transferred into a new 50-ml Falcon tube. A brief centrifugation was performed (1600 rpm for 1 minute), and the pellet was resuspended in 20 ml of RPMI medium. The cell suspension was filtered through a 100-µm mesh and centrifuged at 300 × g for 7 minutes. Red blood cell lysis with Ammonium chloride was performed if the cell pellet was red.

The cells (5×10^5–2×10^6) per FACS tube were washed with Miltenyi buffer (1× PBS, 2 mM EDTA, and 0.5% BSA), centrifuged at 1600 rpm for 5 minutes. Live/Dead (L/D) reagent was then added to label dead cells and incubated for 10 minutes at room temperature. Then, cells were washed and incubated for 15 minutes, room temperature, with an antibody mix staining surface markers. To perform intranuclear and intracellular staining, surface-stained cells were washed, fixed, and permeabilized with Fix/Perm Buffer Set (Biolegend, Amsterdam, The Netherlands) according to the manufacturer's instructions in the dark with specific antibodies (Table 1), purchased from BD Biosciences.

After 40 minutes of incubation on ice or at 4 °C, the fluorescence was washed, and samples were analyzed by a BD Symphony A3 flow cytometer (BD Biosciences) using FlowJo software v10 (Ashland, USA).

Lymphoid Panel		Myeloid Panel	
Antibodies	**Fluorocrome**	**Antibodies**	**Fluorocrome**
Surface antibodies			
Fixiable Viabilty Stain (L/D)	FVS4040 UV	Fixiable Viabilty Stain (L/D)	FVS4040 UV
CD45RA	BV510	CD16	BV510
CD3	BV786	CD163	BV786
CD25	BB515	C D11B	BB515
TIM3	BB700	CD33	BB700
GITR	BV605	CD123	BV605
CD16	BUV615	CD14	BUV615
CD56	RB780	CD11C	RB780
CD39	BUV805	HLA-DR	BUV805
CD8	PE-Cy7	CD3	PE-Cy7
LAG3	APCR700	CD80	APCR700
CD127	BUV737	CD19	BUV737
CCR7	BV711	CD15	BV711
CD279 (PD-1)	RYG586	CD66B	RYG586
CD4	APCH7	CD206	APCH7
CD28	RB670	CD45	BUV395
CD19	PECY5		
CD45	BUV395		
Intracytoplasmic antibodies			
CTLA4	BV421	CD68	BV711
Foxp3	AlexaFluor647		

Table 1: Antibodies and fluorochromes used to detect immune cell populations in MFS TME.

Isolation of Plasma from Whole Blood

Blood samples in EDTA-coated tubes were centrifuged at 1,500 × rpm for 10 minutes at room temperature. Following centrifugation, the clear plasma layer at the top of the tube was carefully aspirated without disturbing the buffy coat or red blood cell layer, and stored at -80 °C.

ELLA

Plasma levels of soluble (s)PD-L1, sLAG-3, sTIM-3, and sCTLA-4 were measured using a custom multiplex cartridge on the Ella automated microfluidic platform (Bio-Techne, Minneapolis, MN, USA). IFN- γ levels were also assessed using the Simple Plex Human IFN-γ (3rd Gen) cartridge, also on the Ella platform. For all analyses, we used 50 µL of the diluted plasma samples (1:2 dilution with the provided diluent). sPD-L1, sLAG-3, sTIM-3, sCTLA-4, and IFN-γ concentrations (pg/mL) were calculated using the manufacturer-calibrated standard curve and analyzed with Ella software.

Statistical analysis

All comparisons between control and treatment groups, or between healthy donors and MFS subjects, were evaluated using a two-tailed t-test. P values < 0.05 were considered statistically significant. Statistical analyses were performed using Prism 9.4 (GraphPad Software, San Diego, CA, USA).

Generative AI statement

AI-based tools were used for language refinement. The content was reviewed, edited, and finalized by the author, who takes full responsibility for the accuracy and originality of the work.

RESULTS

Patients' characteristics

Over the three years of the PhD program, we have collected surgical specimens and plasma from 7 patients (pts) arrived at IRCCS Ospedale Policlinico San Martino-Genova and diagnosed with MFS between 2023 and 2025 (Progetto MultiGenTR CER 534/2020).

The median age at biopsy/surgical intervention was 66 years (range: 53–93), and four patients (57.1%) were male. The most common tumor site was the leg (4/7, 57.1%), followed by the chest wall (2/7, 28.6%) and the pelvis (1/7, 14.3%). Most tumors were high grade (G3, 6/7, 85.7%), while one case was graded as G2. Biopsies were obtained from the primary tumor in three patients (42.9%), from local relapse in three patients (42.9%), and from metastatic lesions in one patient (14.3%).

Apart from surgery, three patients (42.9%) did not receive any other therapy, whereas two patients received chemotherapy and two received radiotherapy prior to specimen collection. (Table 2)

Tumor samples were analyzed by NGS Archer™ FUSIONPlex™ Sarcoma v2 (Integrated DNA Technologies, Inc.) for the presence of major mutations. No mutation or gene fusions were detected in those patients by NGS Archer™ FUSIONPlex™ Sarcoma v2.

Characteristic	**Value**
Number of patients	7
Age, years	Median 66 (range 53–93)
Sex	
Male	4 (57.1%)
Female	3 (42.9%)
Tumor site	
Leg	4 (57.1%)
Chest wall	2 (28.6%)
Pelvis	1 (14.3%)
Tumor grade	
G2	1 (14.3%)
G3	6 (85.7%)
Site of biopsy	
Primary tumor	3 (42.9%)
Local relapse	3 (42.9%)
Metastasis	1 (14.3%)
Pre-treatment	
None	3 (42.9%)
Chemotherapy	2 (28.6%)
Radiotherapy	2 (28.6%)

Table 2: Patients' characteristics

Establishment of primary cell lines and in vitro characterization

Fresh surgical specimens or biopsies were immediately transported to the laboratory, mechanically minced into small fragments, and incubated for 3 hours at 37°C in agitation in a solution of HBSS containing 5 mg/ml collagenase I. The single cell suspension was seeded onto monolayer plates. After the 10^{th} passage, cells seem to modestly enhance proliferation. Cells grow in adherence to the flask and show a spindle-shaped, fibroblast-like morphology like MFS cells within the tumor. So far, we have generated three stable primary cell lines: MFS001, MFS002, and MFS003 (Figure 1).

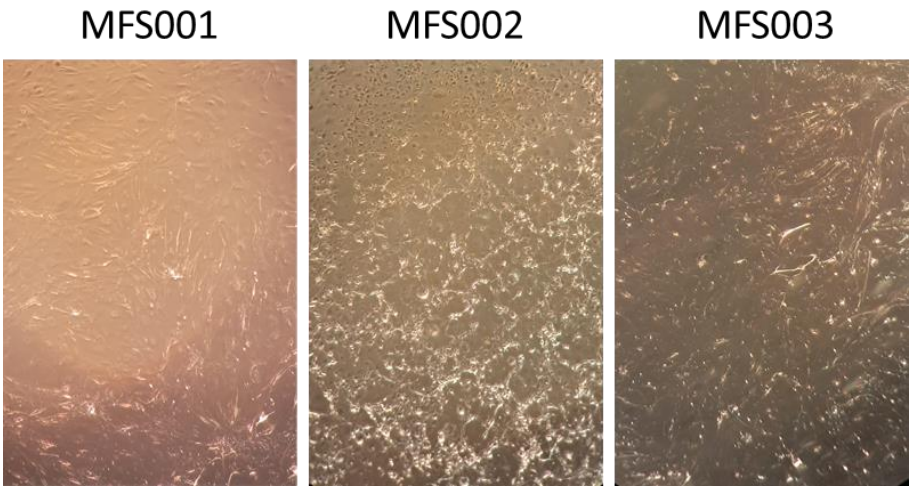

Figure 1: Representative images of MFS primary cell lines after spontaneous immortalization, captured using an inverted microscope (5X magnification), showing their morphological features.

The culture was maintained for 30 passages, and the morphology did not change significantly over time; cells showed abundant cytoplasm and prominent nuclei. MFS001 and MFS002 primary cell lines, seeded at 5,000–10,000 cells per well in 96-well plates, were monitored by the CellTiter 96® AQueous One Solution assay to evaluate cell proliferation. As shown in Figure 2, all cell lines display an increase in OD over time, indicating cell growth or increased metabolic activity, although with distinct kinetic profiles. Indeed, MFS001 shows a progressive increase from baseline to 168 h, with a clear rise at 72 h and a further, albeit moderate, increase at 168 h; MFS002 exhibits the most pronounced growth, with a significant increase already at 72 h and a further rise at 168 h, reaching the highest OD values among the analyzed cell lines; MFS003 displays a more moderate increase, peaking at 72 h and followed by a trend toward stabilization or a slight decrease at 168 h, suggesting slower growth or adaptive changes over time. These data highlight functional heterogeneity among MFS-derived cell lines, with MFS002 displaying a higher proliferative capacity, whereas MFS003 show more limited long-term growth. This heterogeneity is consistent with the known biological variability of MFS and underscores the importance of using multiple representative models to investigate tumor behavior and therapeutic responses.

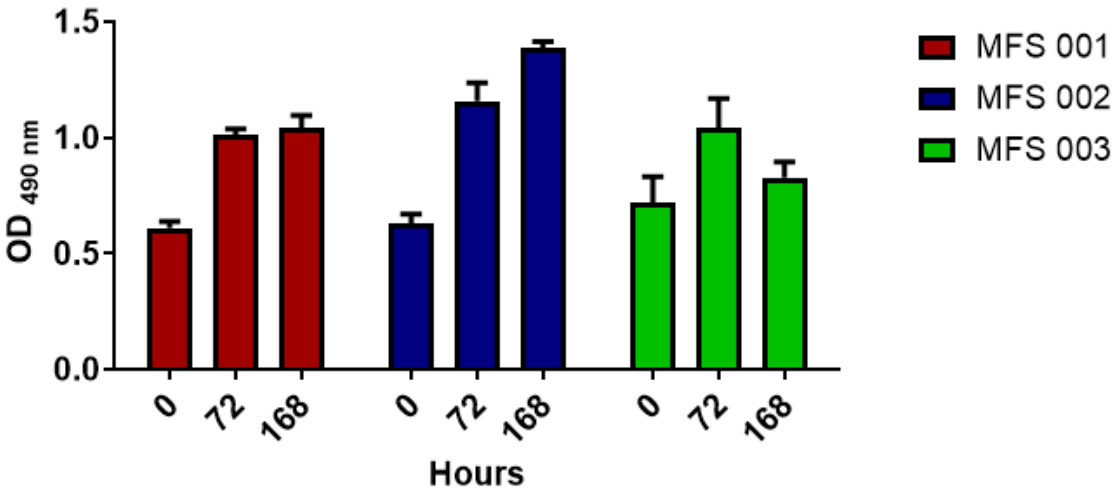

Figure 2: Proliferation assay of MFS001, MFS002, and MFS003 growing in adherence. Data are expressed as mean and standard deviation

To characterize MFS primary cell lines, we checked by flow cytometry the surface expression of different molecules: HLA class I/II, immune checkpoint ligand PD-L1, mesenchymal CD105, and stromal marker FAP. HLA class I molecules are essential for presenting endogenous tumor antigens to $CD8^+$ cytotoxic T lymphocytes; their quantitative or qualitative loss represents a key mechanism of tumor immune evasion in cancer [65]. PD-L1, an immune checkpoint ligand to PD-1, was detected in approximately 18 % of MFS cases, confirming that MFS can express the immune checkpoint ligand, and that expression varies by subtype [17,66]. CD105 (Endoglin) is expressed in human sarcoma cell lines and is associated with enhanced proliferative capacity compared to carcinoma cells [67,68]. Fibroblast activation protein (FAP), a membrane-bound serine protease predominantly expressed in cancer-associated fibroblasts, is highly expressed in the stromal compartments of soft tissue and bone sarcomas [69].

As shown in Table 3, primary cell lines show similarities to human fibroblasts, particularly in the expression of CD105 and FAP. PD-L1, is expressed only in MFS001 and MFS002 cell lines and is absent in MFS003. Conversely, all MFS cell lines tested express high HLA-class I, but not HLA-class II. Treatment with human interferon (IFN)-γ upregulated the expression of HLA class I and, to a lesser extent, HLA class II, but did not induce PD-L1 expression in primary MFS cell lines. These results indicate that primary MFS cell lines retain a fibroblastic phenotype while maintaining strong HLA class I–mediated antigen presentation potential. The limited basal expression of PD-L1 and absence of HLA class II suggest a relatively low intrinsic immunosuppressive profile, which can be partially modulated by IFN-γ. Collectively, these findings highlight the immunophenotypic characteristics of MFS cells and their potential responsiveness to immune stimuli.

Primary Cell line	CD105	FAP	HLA-class I	HLA-class II	PD-L1
MFS001	73.2	93.9	49.7	2	12.9
MFS002	42.7	88.9	11.5	3.5	12.9
MFS003	80	76.6	32	0	0
Human Fibroblasts	84.2	86.5	42.7	3.9	7.5

Table 3: Percentages of MFS primary cell lines and human fibroblasts positive for CD105, FAP, HLA-class I and -class II, and PD-L1

Characterization of the TME

We analyzed the composition of the TME by flow cytometry on fresh tumor samples using two multiparametric panels specific for lymphoid and myeloid cell populations. These panels, previously validated on peripheral blood mononuclear cells and human tumor samples, enabled comprehensive identification of all selected immune populations through a detailed gating strategy. Tumor cell suspensions stained with different fluorochrome-conjugated antibodies were analyzed using a BD Symphony A3 flow cytometer. The gating strategy used to identify lymphoid and myeloid populations is based on a series of sequential plots (Figure 3). The initial dot plot allows evaluation of overall data quality by visualizing all acquired cells in the sample, and a region containing lymphoid- and myeloid-sized cells is selected based on forward scatter (FSC) and side scatter (SSC) parameters. Within this population, $CD45^+$ live/dead-negative (L/D^-) cells are identified to exclude debris, dead cells, and non-hematopoietic components. The next two gating steps are dedicated to the selection of single-cell events, discriminating singlets from doublets within the $CD45^+$ L/D^- population. Doublets consist of two physically adjacent cells that pass almost simultaneously through the laser interrogation point and are incorrectly recorded as a single event. The singlet gate defined using FSC-Area (FSC-A), which reflects overall cell size, and FSC-Height (FSC-H), which reflects the peak scattering signal, allows exclusion of these artifactual events, ensuring that only properly acquired single cells are included in the analysis. Among live, single $CD45^+$ cells, the first distinction identifies the major lymphoid populations: $CD19^+$ B cells and $CD3^+$ T cells. Within the T-cell compartment, $CD3^+$ cells are further subdivided into helper T cells ($CD4^+$) and cytotoxic T cells ($CD8^+$). For both subsets, the maturation status discriminated against three main functional subsets based on the combined expression of CCR7 and CD45RA: naïve, central memory, and effector memory T cells. Specifically, Naive T cells represent mature lymphocytes that have not yet encountered their specific antigen. $CD4^+$ T central memory cells are long-lived and highly proliferative, capable of recirculating between blood and lymphoid organs to mount responses upon repeated antigen exposure. $CD4^+$ Teffector memory cells are poised for rapid effector responses, producing cytokines such as IL-2 and

IFN-γ. $CD8^+$ T central memory cells exhibit high proliferative capacity and contribute to long-term immunological memory. $CD8^+$ T effector memory cells rapidly exert effector functions by producing cytotoxic mediators, including IFN-γ, TNF-α, granzymes, and perforin. Tregs are identified as $CD127^-$ $CD25^+$ $FoxP3^+$, representing a specialized subset of $CD4^+$ T lymphocytes that maintain immune homeostasis by suppressing excessive or autoreactive immune responses, which play a key role in suppressing effector T-cell responses and promoting tumor immune tolerance [53]. Immune checkpoint receptor expression on T cells, together with their maturation status, allowed the identification of exhausted T-cell populations, which exhibit impaired cytotoxic function and are unable to efficiently eliminate tumor cells. From the $CD45^+CD3^-CD19^-$ population, NK cells were identified as $CD45^+CD3^-CD56^+$ cells. NK cell subsets were further defined based on CD16 expression, distinguishing $CD56^{bright}CD16^-$ cytokine-producing NK cells and $CD56^{dim}CD16^+$ highly cytotoxic NK cells. From the $CD45^+CD3^-CD19^-$ population, the myeloid compartment was identified. Within this population, macrophages were identified as $HLA\text{-}DR^+CD68^+$ cells and further subdivided into M1-like ($CD206^-CD163^-$) and M2-like ($CD206^+CD163^+$) subsets. M1-like macrophages exhibit pro-inflammatory and antitumoral activity through the production of cytokines such as TNF-α and IL-12 and by promoting T-cell activation, whereas M2-like macrophages display immunosuppressive and pro-tumoral functions, contributing to tissue remodeling, angiogenesis, and inhibition of adaptive immune responses [70]. Monocytes ($HLA\text{-}DR^+CD14^+$) act as precursors of macrophages and dendritic cells and participate in innate immune responses through phagocytosis and cytokine production, which contribute to inflammatory regulation and cellular recruitment within the TME [71]. Dendritic cells ($HLA\text{-}DR^+CD14^-$) are professional antigen-presenting cells that initiate and regulate adaptive immune responses by activating T lymphocytes [51]. From the $HLA\text{-}DR^-CD14^-$ population, myeloid-derived suppressor cells (MDSCs) were identified as $CD33^+CD11b^+$ cells. These cells exert potent immunosuppressive activity by inhibiting T-cell proliferation and function. Granulocytic MDSCs (PMN-MDSCs; $CD15^+CD14^-$) suppress immune responses mainly through the production of reactive oxygen species, whereas monocytic MDSCs (M-MDSCs; $CD15^-CD14^+$) mediate suppression via arginase-1, nitric oxide, and immunosuppressive cytokines, and are known to inhibit T- and NK-cell function, interfere with antigen presentation, and contribute to primary and acquired resistance to immune checkpoint inhibitors [72].

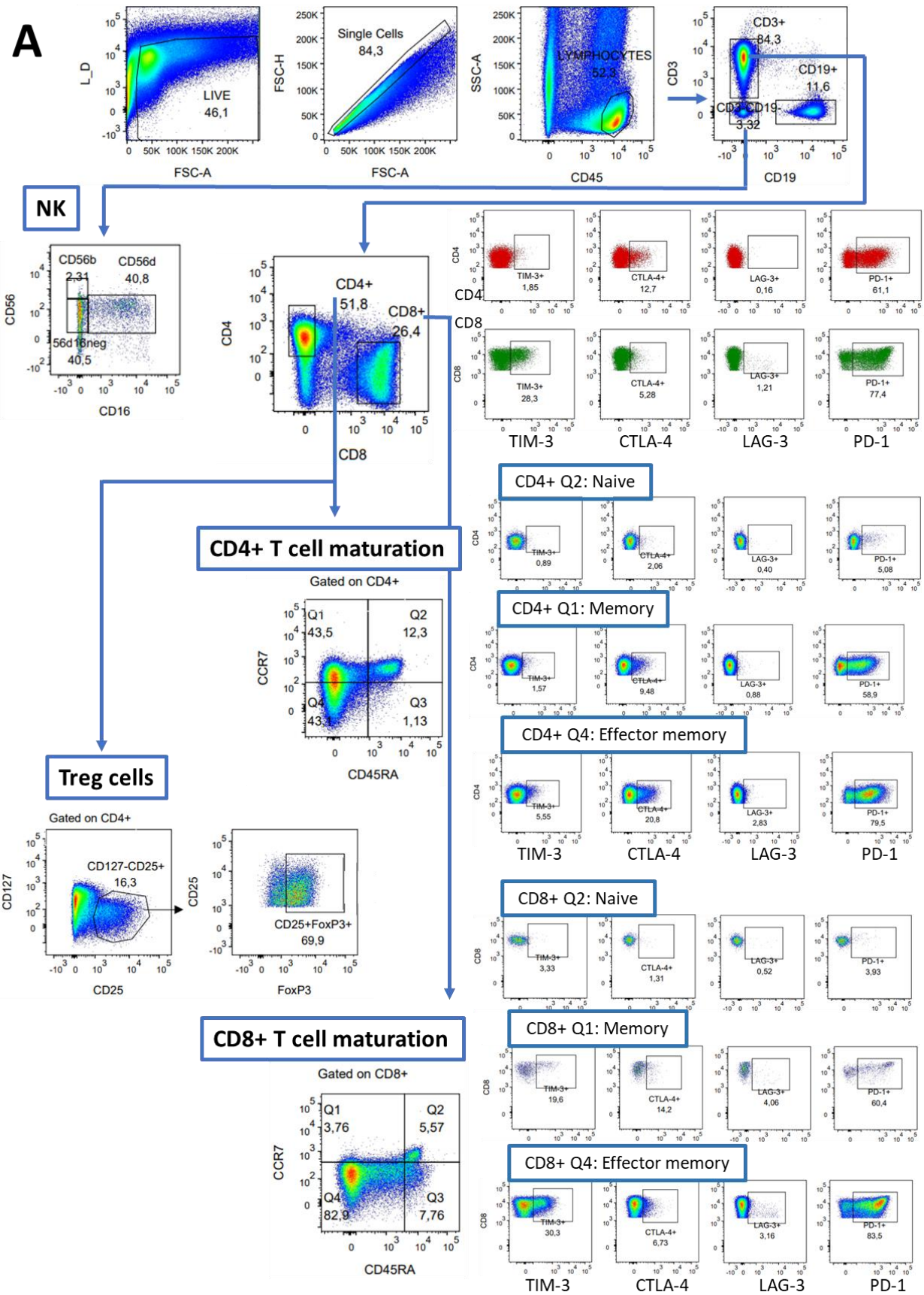
A
L_D
LIVE
46,1
FSC-A
FSC-H
Single Cells
84,3
SSC-A
LYMPHOCYTES
52,3
CD45
CD3
CD3+
84,3
CD19+
11,6
CD3-CD19-
3,32
CD19
NK
CD56
CD56b
2,31
CD56d
40,8
56d16neg
40,5
CD16
CD4
CD4+
51,8
CD8+
26,4
CD8
TIM-3+
1,85
CTLA-4+
12,7
LAG-3+
0,16
PD-1+
61,1
TIM-3+
28,3
CTLA-4+
5,28
LAG-3+
1,21
PD-1+
77,4
TIM-3
CTLA-4
LAG-3
PD-1
CD4+ T cell maturation
Gated on CD4+
CCR7
Q1
43,5
Q2
12,3
Q4
43,1
Q3
1,13
CD45RA
CD4+ Q2: Naive
TIM-3+
0,89
CTLA-4+
2,06
LAG-3+
0,40
PD-1+
5,08
CD4+ Q1: Memory
TIM-3+
1,57
CTLA-4+
9,48
LAG-3+
0,88
PD-1+
58,9
CD4+ Q4: Effector memory
TIM-3+
5,55
CTLA-4+
20,8
LAG-3+
2,83
PD-1+
79,5
TIM-3
CTLA-4
LAG-3
PD-1
Treg cells
Gated on CD4+
CD127
CD127-CD25+
16,3
CD25
CD25+FoxP3+
69,9
FoxP3
CD8+ Q2: Naive
TIM-3+
3,33
CTLA-4+
1,31
LAG-3+
0,52
PD-1+
3,93
CD8+ T cell maturation
CD8+ Q1: Memory
TIM-3+
19,6
CTLA-4+
14,2
LAG-3+
4,06
PD-1+
60,4
Gated on CD8+
CCR7
Q1
3,76
Q2
5,57
Q4
82,9
Q3
7,76
CD45RA
CD8+ Q4: Effector memory
TIM-3+
30,3
CTLA-4+
6,73
LAG-3+
3,16
PD-1+
83,5
TIM-3
CTLA-4
LAG-3
PD-1

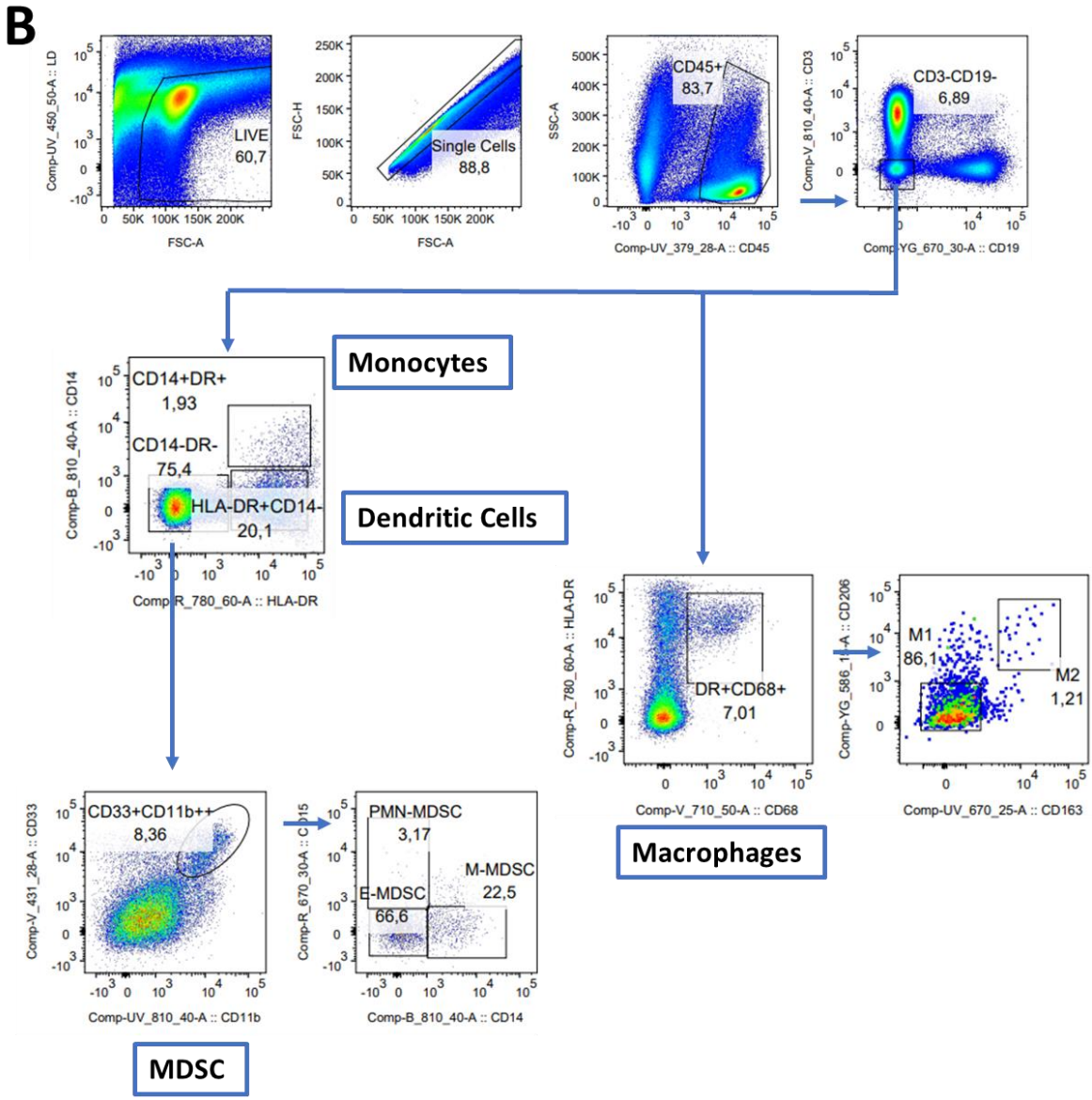

Figure 3: Representative flow cytometric analysis of TME immune cells acquired on a BD FACSymphony A3 and analyzed using FlowJo v10. A: Cells were first gated based on forward and side scatter to exclude debris. Single, live (LD^-) $CD45^+$ cells were then identified for downstream analysis. Within the $CD45^+$ population, B cells ($CD19^+$) and T cells ($CD3^+$) were analyzed, and T cells were further subdivided into $CD4^+$ and $CD8^+$ subsets. T cell maturation was assessed using CCR7 and CD45RA expression. Mature T cells expressing immune checkpoint receptors LAG-3, TIM-3, CTLA-4, and PD-1 are identified. Regulatory T cells (Tregs) were identified within the $CD4^+$ subset as $CD127^-$ $CD25^+$ $FoxP3^+$. Natural killer (NK) cells were identified as $CD3^-$ $CD19^-$ and further subdivided into CD56^bright $CD16^-$ and CD56^dim $CD16^+$ subsets. B: From $CD3^-$ $CD19^-$ gating, we identified: macrophages as HLA-DR^+ $CD68^+$ cells and further subdivided into M1-like ($CD206^-$ $CD163^-$) and M2-like ($CD206^+$ $CD163^+$) subsets, monocytes (HLA-DR^+ $CD14^+$) and dendritic cells (HLA-DR^+ $CD14^-$). From HLA-DR^- $CD14^-$ cells, myeloid-derived suppressor cells (MDSCs) were identified as $CD33^+$ $CD11b^+$ and further subdivided into granulocytic (PMN-MDSC, $CD15^+$ $CD14^-$) and monocytic (M-MDSC, $CD15^-$ $CD14^+$) subsets.

Of the seven patients enrolled in the study, complete TME analyses were successfully performed for three patients (MFS001, MFS002, and MFS007). For patient MFS003, only a biopsy was available, which did not provide sufficient material for analysis. Similarly, tissue samples from patient MFS004 and MFS005 were limited, preventing complete TME characterization; however, they allowed the identification of T-cell populations and immune checkpoint receptor expression. For patient MFS006, only the myeloid panel could be applied, as very few $CD45^+$ cells were detected. Limited tissue availability therefore represented the main constraint in this study.

Results demonstrated a TME containing a variable proportion of living, infiltrating $CD45^+$ cells, ranging from 13.3% in MFS007 to 87.4% in MFS005 (Table 4). The only exception was MFS006, which showed only 4.05% of living $CD45^+$ cells. T cells and their subsets were clearly detectable in most MFS specimens. Immune checkpoint receptors were expressed on both $CD4^+$ and $CD8^+$ T cells, with PD-1 being the most highly expressed receptor, showing relatively consistent levels across different tumor specimens.

T-cell maturation was analyzed in detail only in MFS001, MFS002, and MFS007. While MFS001 showed an almost equal distribution of $CD4^+$ central and effector memory cells over CD3+ cells, in MFS002 and MFS007, the $CD4^+$ compartment was predominantly effector memory. A large proportion of both central and effector memory $CD4^+$ T cells expressed PD-1, and in MFS002 and MFS007, also TIM-3, suggesting the presence of a functionally exhausted T-cell population within the TME. Particularly, in MFS007, a large proportion of both central and effector memory $CD4^+$ T cells also expressed CTLA-4, indicating a highly exhausted phenotype.

Regarding the $CD8^+$ T-cell compartment, the three tumors contained high proportions of effector memory $CD8^+$ T cells within the $CD3^+$ population, with most cells co-expressing PD-1 and TIM-3 (MFS001) or CTLA-4 (MFS002 and MFS007), indicative of an exhausted phenotype.

Among $CD4^+$ T cells, Tregs were detected at 11.4–24.3% in tumors, with MFS007 showing the highest percentage. These findings reveal a markedly immunosuppressive TME, characterized by a high frequency of Tregs and $CD8^+$ T cells with an exhausted phenotype, exhibiting elevated expression of immune checkpoint molecules.

Myeloid cells were successfully assessed in samples from patients MFS001, MFS006, and MFS007. Our analysis revealed variable proportions of dendritic cells, ranging from 1.38% to 5.8% of the $CD45^+$ population. Monocytes and macrophages were predominantly detected in MFS006 and MFS007. Among tumor-associated macrophages, M1-like subsets were more abundant in MFS001 and MFS006, whereas MFS007 was characterized by a predominance of M2-like macrophages, further underlying the immunosuppressive, exhausted TME of this patient.

Finally, myeloid-derived suppressor cells (MDSCs) within the $CD45^+$ population were detectable in all three tumors, with higher frequencies observed by MFS007. Among MDSC subsets, monocytic

MDSCs represented the predominant population. Overall, these findings further support the presence of a strongly immunosuppressive myeloid compartment, especially in MFS007, potentially contributing to impaired antitumor immune responses within the TME.

	MFS001	MFS002	MFS004	MFS005	MFS006	MFS007
CD45+	52 .3	21	50.3	87 .4	4 .05	13 .3
Lymphocytes						
T	84 .3	85 .2	38.5	86		61
B	11 .6	0 .37				0,17
NK	1,4	6,53	40.5	1.89		8,32
T cells						
CD4+	51 .8	34 .6	64.4	49 .6		54,5
CD4+ TIM-3	1 .83	52 .3	93 .2	0 .16		45,5
CD4+ CTLA-4	12 .7	4 .72		1 .13		27,7
CD4+ LAG-3	0 .16	10 .8	1 .57	1 .05		10
CD4+ PD-1	61 .1	93 .2	98 .8	88 .3		93,6
CD8+	26 .4	55 .8	26.5	36 .7		27,1
CD8+ TIM-3	28 .3	86 .3	89 .2	0 .11		15,5
CD8+ CTLA-4	5 .28	9 .81		0 .33		40,8
CD8+ LAG-3	1 .21	12 .8	0 .64	0 .65		3,74
CD8+ PD-1	77 .4	96 .8	86	92 .7		83,5
CD4+ T cell maturation						
Naive	12 .3	0 .7				0,34
Central Memory	43 .5	12 .4				4,16
Central Memory TIM-3	1 .57	39 .4				65,6
Central Memory CTLA-4	9 .48	18 .7				30,5
Central Memory LAG-3	0 .4	11 .3				36,5
Central Memory PD-1	58 .9	90 .9				80,4
Effector Memory	43 .1	86				95
Effector Memory TIM-3	5 .55	56 .7				45
Effector Memory CTLA-4	20 .8	3 .61				27,8
Effector Memory LAG-3	1 .38	17 .3				6,96

Effector Memory PD-1	79 .5	95 .6				94,9
CD8+ T cell maturation						
Naive	5 .57	0 .29				0,41
Central Memory	3 .76	0 .87				2,98
Central Memory TIM-3	19 .6	85 .2				31,7
Central Memory CTLA-4	14 .2	94 .1				77,2
Central Memory LAG-3	4 .06	68				21,8
Central Memory PD-1	60 .4	83 .4				88,1
Effector Memory	82 .9	81 .4				84,8
Effector Memory TIM-3	30 .3	91 .3				76,3
Effector Memory CTLA-4	6 .73	8 .01				38,4
Effector Memory LAG-3	3 .16	33 .9				4,03
Effector Memory PD-1	83 .5	97 .5				88,3
Myeloid cells						
Monocytes	0.13				9.89	18
Dendritic cells	1.38				5.8	3.17
Macrophages	0.48				3.8	17.2
TAM- M1	86 .1				37 .9	12
TAM-M2	1 .21				21 .8	69 .7
Immune suppressive cells						
T-reg	11 .4	17 .86				24,3
MDSC	0.43				1.89	7.8
PMN-MDSC	3 .19				6 .11	0 .36
M-MDSC	22 .6				34	71 .9

Table 4: TME: Percentages of immune cell populations identified in each MFS tumor specimen. Lymphocytes are expressed as a proportion of $CD45^+$ cells; $CD4^+$ and $CD8^+$ T cells and their maturation subsets are expressed as a proportion of $CD3^+$ T cells; myeloid cells and MDSC are expressed as a proportion of $CD45^+$ cells; Treg cells are expressed as a proportion of CD4+ cells.

Analysis of soluble plasma markers

To provide complementary information about systemic immune activation, immune dysfunction, and tumor–host interactions, we performed ELISA, using the Ella automated microfluidic platform to detect IFN-γ and soluble immune checkpoint receptors in the plasma of MFS patients. Plasma samples were obtained from peripheral blood collected at the time of surgical intervention or diagnostic biopsy. IFN-γ is a key cytokine produced primarily by activated T cells and NK cells and plays a central role in anti-tumor immunity [73]. We observed significantly higher amounts of IFN-γ in MFS patients compared to healthy controls, possibly reflecting chronic immune activation, which can contribute to immune exhaustion (Figure 4A). This occurs when cells secrete IFN-γ but fail to mount effective cytotoxic responses, contributing to persistent systemic levels. Indeed, discrete amounts of soluble immune checkpoints were detected in plasma from MFS patients, with LAG-3 and TIM-3 being the most abundant (Figure 4B). This data further corroborates the possibility of endogenous immune activation, chronic T-cell activation, induction of checkpoint expression, and shedding [74].

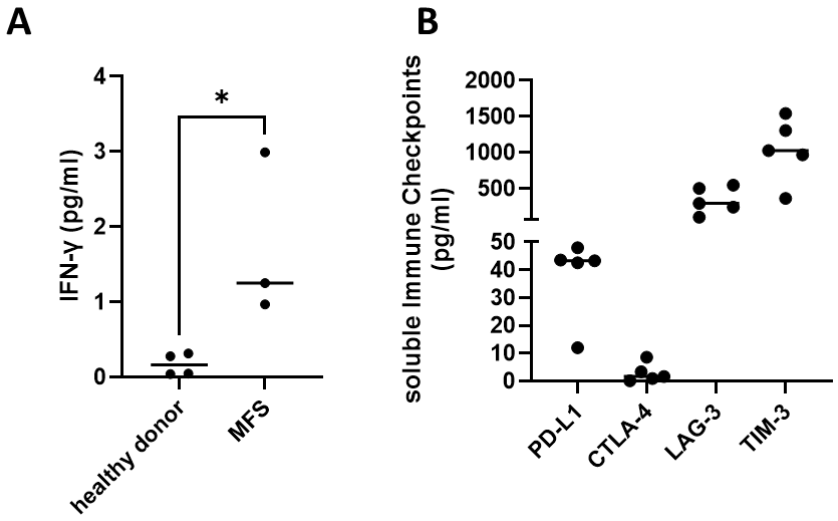

Figure 4: Bar graphs showing A: IFN-γ levels in healthy donors and MFS patients, and B: soluble immune checkpoints: sPD-L1, sCTLA-4, sLAG-3, and sTIM-3 levels in MFS patients. Results are expressed as mean by standard deviation. *$p<0.05$

Analysis of TP53 mutational and functional status

MFS primary cell lines show TP53 alteration

Since patient MFS003 had a history of multiple cancers, he was referred to the genetics department, where he was diagnosed with Li-Fraumeni syndrome, a hereditary cancer-predisposition disorder caused by a pathogenic mutation in the TP53 gene. Genomic alterations affecting TP53 represent the most frequent molecular abnormalities observed in Li-Fraumeni syndrome [17]. Based on this evidence, we assessed the basal protein levels of p53 in total primary MFS cell lysates. As shown in Figure 5, Western blotting revealed high p53 expression across all cell lines analyzed, with the highest levels observed in MFS003 and S148 primary cells. The MFS002 cell line displayed a molecular weight lower than the canonical 53 Kda of p53, consistent with the expression of a p53 isoform. S11 primary cell line showed no p53 expression. We also analyzed p21 protein expression in all MFS samples. P21 is a cyclin-dependent kinase inhibitor that plays a key role in cell cycle regulation; it is a major downstream effector of p53 [75]. In our western blotting analysis, we also detected high constitutive levels of p21. Under normal conditions, p53 protein levels are low due to rapid degradation, and constitutive p53 expression may be suggestive of alterations of p53 functionality, potentially a missense mutation in the TP53 gene [76,77]; constitutive p21 expression may reflect active p53 signaling, or p53-independent p21 regulation [78].

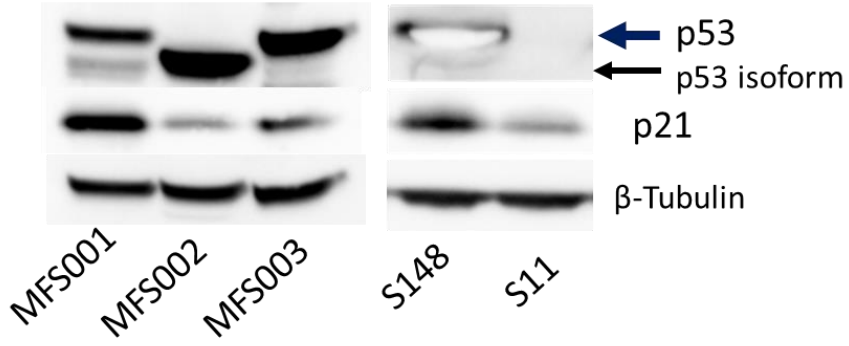

Figure 5: Western blotting analysis showing p53, p21, and β-tubulin protein expression in MFS primary cell lines

To assess the TP53 status in MFS cell lines, we took advantage of functional analysis of separated alleles in yeast (FASAY) (Figure 6) that exploits homologous recombination in the S. Cerevisiae yIG397 strain to generate a plasmid expressing the entire p53 coding sequence deriving from the MFS primary cell line (see Materials and Methods); the yIG397 strain at the genomic level harbors the ADE2 reporter gene, involved in adenine biosynthetic pathway under the control of a p53-responsive element. When cells express a p53 (i.e., wild-type) that functions as a transcription factor

in yeast, the ADE2 gene is expressed with consequent formation of white normal-sized colonies (see details in Materials and Methods); conversely, cells containing a mutant P53 protein grow as small red colonies due to the accumulation of a colored intermediate in the adenine biosynthetic pathway. The functional status of the TP53 gene is therefore defined by the percentage of red colonies over the total number of white and red colonies. Consequently, when analyzing the TP53 status of a cell line, the presence of wild-type p53 is expected to yield 85–100% white colonies. In contrast, a non-functional TP53 mutation in the heterozygous state typically results in approximately 50% small red colonies, whereas homozygous TP53 mutations lead to 100% small red colonies.

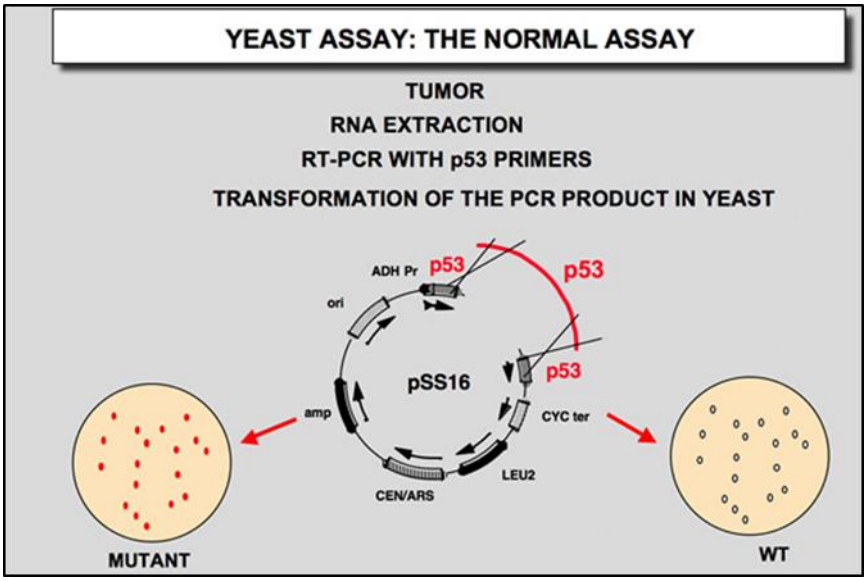

Figure 6: Schematic representation of the workflow of the functional analysis of separated alleles in yeast (FASAY).

RNA extracted from MFS primary cell lines was reverse-transcribed, and P53 was amplified by PCR. Among all the cell lines tested, S11 did not show the specific P53 PCR product (Figure 7), confirming the absence of P53 also at mRNA level, and suggesting a deletion of TP53 gene, supported by western blotting analysis results.

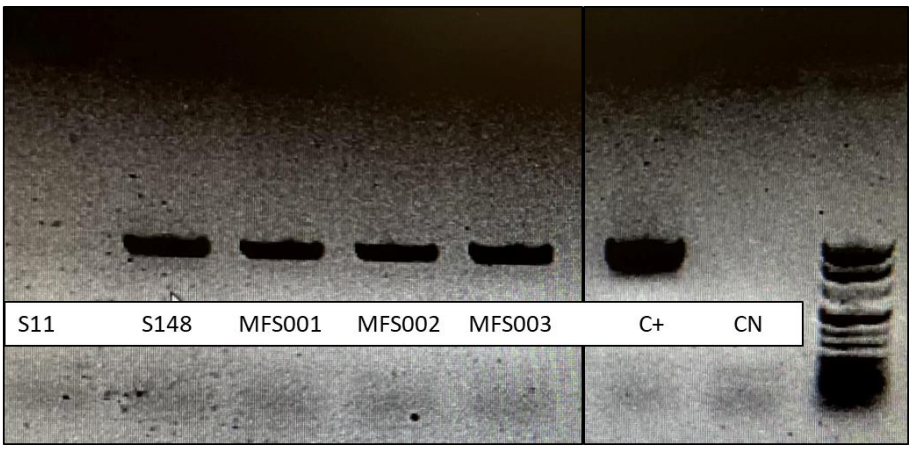

Figure 7: P53-specific PCR products separated in 1% agarose gel stained with SYBR Safe, showing, from left to right: S11, S148, MFS001, MFS002, MFS003, positive, negative control, and molecular weight marker (VIII Roche).

The results of the FASAY demonstrated the presence of a wild-type TP53 gene in MFS001 (14%) and MFS002 (10%) cell lines; conversely, TP53 mutation (s) are present at heterozygous and homozygous states in MFS003 (68%) and S148 (100%) cell lines, respectively (Table 5).

Cell line	Red colonies/total	p53 functional status
MFS001	14%	Wild-type
MFS002	10%	Wild-type
MFS003	68%	Mutated/Hypofunctional
S148	100%	Mutated/not functional

Table 5: FASAY results showing percentages of red colonies and identifying p53 functional status

P53 PCR products were analyzed at the molecular level by Sanger sequencing, confirming the presence of a wild-type TP53 gene in MFS001 and MFS002 cell lines, and identifying mutations in the MFS003 (heterozygous R213Q) and in the S148 cell line (homozygous R280K) (Figure 8). Sanger sequencing highlighted the presence of P53 codon 72 polymorphisms (Table 6). In conclusion, out of 5 primary cell lines derived from MFS patients, 3 (3/6, 60%) showed an alteration of the TP53 gene, confirming the previously reported alteration frequency in MFS tumors.

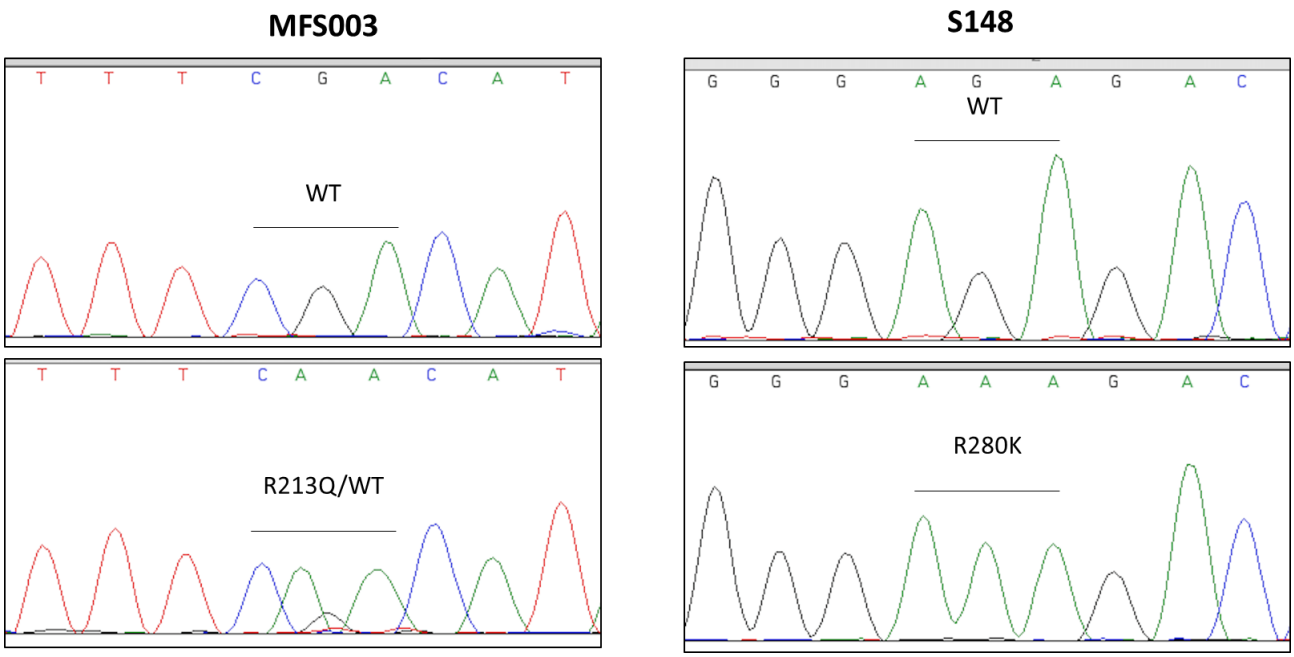

Figure 8: Sanger sequencing showing the heterozygous mutation R213Q in MFS003 and the homozygous R280K mutation in S148 primary MFS cell lines.

Cell line	P53 status	Codon 72 polymorphism
MFS001	Wild-type	P72P/P72R
MFS002	Wild-type	P72R
MFS003	R213Q (heterozygous)	P72R
S148	R280K (homozygous)	P72R

Table 6: P53 status and codon72 polymorphism in MFS primary cell lines

Assessment of p53 Pathway Activation in MFS Cell Lines Following Irradiation

To evaluate p53 and p53–target proteins' functionality, cells were exposed to irradiation. We selected the cell cycle arrest CDKN2A/p21 protein as the major p53-target protein, induced in response to DNA damage, where it promotes cell cycle arrest (at the G1/S checkpoint) for DNA repair or activation of senescence and apoptosis pathways [79]. Plated cells were irradiated with 10 Gy and returned to the incubator; cell lysates were collected at 2, 4, and 8 hrs post-irradiation. Two cell lines, representative of wild-type and heterozygous mutant TP53 (wild-type/R213Q), were selected: MFS002 and MFS003. Western blot analysis showed generally high levels of p53 and p21 proteins in both untreated cell lines, likely reflecting a partial cell-cycle arrest consistent with the reduced proliferation rate of the cells. Interestingly, the MFS002 cell line showed the presence at the basal level of a distinct p53 isoform from the canonical 53 KDa protein. Moreover, p53 (i.e., 53 Kda variant) and p21 proteins were clearly up-regulated as early as 2 hours after irradiation in MFS003;

this induction, but to a lesser extent, was also present in MFS002 (Figure 9). Concurrently, the level of the distinct p53 isoform in MFS002 cell line appeared largely unaffected by the treatment. All together, these results suggested an appreciable activation of the p53 pathway only in MFS003 cells, despite the presence of the heterozygous R213Q TP53 mutation; conversely, the weak induction of p53 and p21 proteins in the MFS002 cell line, along with the presence of a different p53 isoform, might indicate the presence of an altered p53 pathway that needs further investigation.

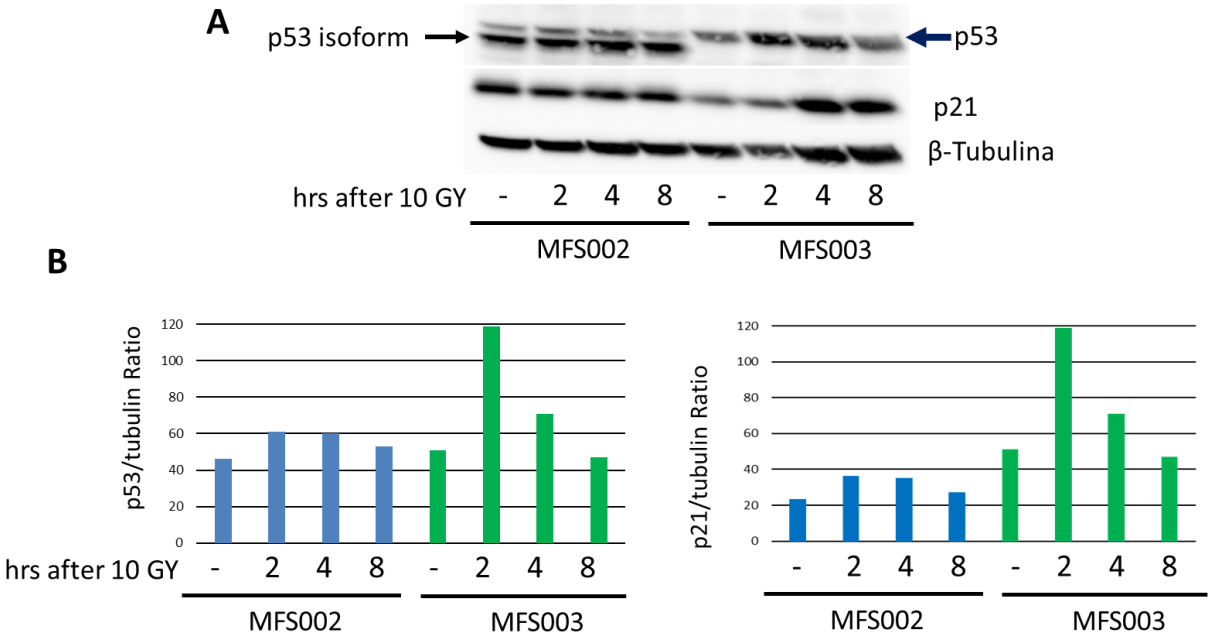

Figure 9: Western blot and densitometric analyses of MFS001 and MFS003 cell lysates from control (un-irradiated) and irradiated cells kept in culture for 2, 4, and 8 hours after irradiation. A: The thick arrow indicates p53 protein, while the thin arrow p53 isoform. B: Densitometric analysis: Histograms show the quantification of band intensity expressed as a percentage p53 over β-tubulin (left) and p21 over β-tubulin (right)

Sensitivity to chemotherapeutic agents in 2D culture

The sensitivity of primary MFS cell lines to chemotherapeutic agents commonly used in clinical practice was investigated using cell viability assays in 2D monolayer cultures. Primary MFS cells were seeded at a density ranging from 5,000 to 10,000 cells per well, depending on the growth characteristics of each cell line. Cultures were therefore treated with increasing concentrations of doxorubicin or palifosfamide and incubated for a total of 7 days. Cell proliferation was then evaluated using the CellTiter 96® AQueous One Solution assay. In an initial experimental phase, experiments performed with clinical drug formulations revealed resistance to ifosfamide and only limited sensitivity to doxorubicin. For this reason, subsequent analyses were carried out using purified active compounds to more accurately assess drug-specific effects. Under these conditions, all tested MFS

cell lines exhibited a clear dose-dependent decrease in cell viability after 7 days of treatment with both doxorubicin and palifosfamide (Figure 10).

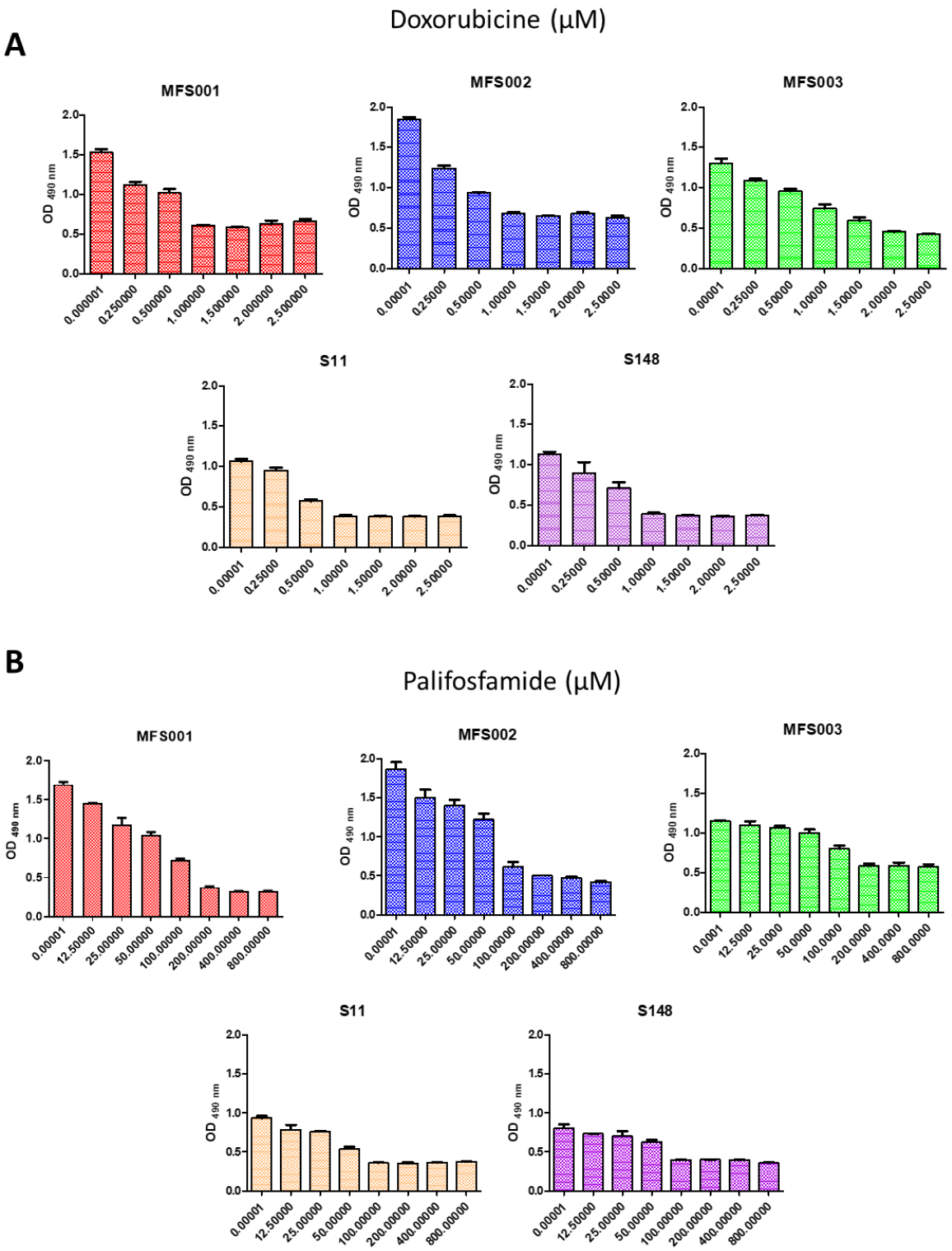

Figure 10: Cell viability, evaluated at OD_{490nm}, using CellTiter 96® AQueous One Solution for MFS001, MFS002, MFS003, S11, and S148 in response to different dosages of Doxorubicin and Palifosfamide. Data are expressed as mean and standard deviation.

IC_{50} values were calculated by normalizing the data to untreated control cells. They indicated a higher sensitivity to doxorubicin, with inhibitory concentrations in the sub µM range, whereas higher µM concentrations of palifosfamide were required to achieve a comparable reduction in cell viability (Figure 11, Table 7). Although some variability in drug response was observed among the different MFS cell lines, these results confirm the cytotoxic activity of both chemotherapeutic agents in vitro and highlight differences in chemosensitivity across primary tumor-derived cells.

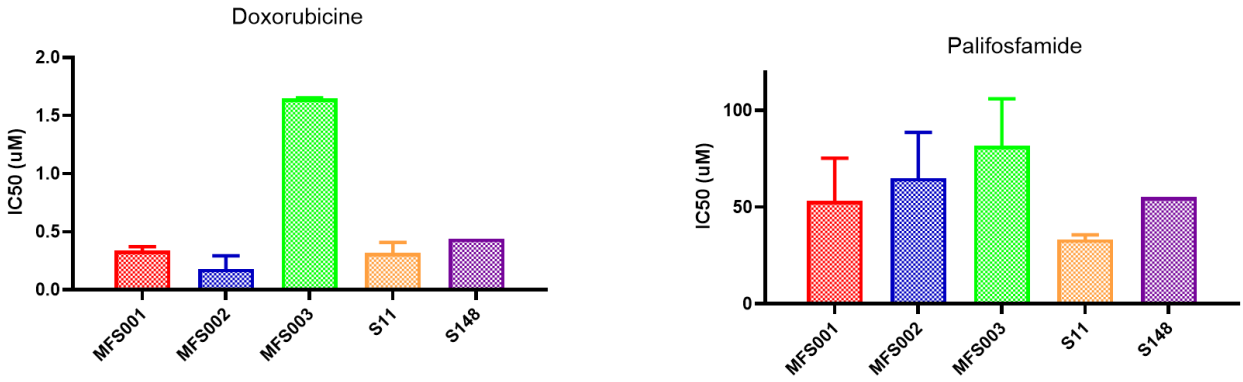

Figure 11: IC_{50} values (µM) were determined based on cell proliferation in 96-well plates of MFS cells grown in monolayer, in the presence or absence of doxorubicin and palifosfamide after 1 week of treatment. Data are expressed as mean and standard deviation.

	DOXORUBICIN IC50 (µM)	**PALIFOSFAMIDE IC50 (µM)**
Cell line	*Mean ± SD*	*Mean ± SD*
MFS 001	0.33 ±0.035	53.2 ± 22.2
MFS 002	0.18 ± 0.113	65 ± 23.7
MFS 003	1.65 ± 0.007	81.7 ± 24.4
S11	0.32 ±0.091	33.3 ± 2.5
S148	0.44	55.3

Table 7: IC_{50} concentrations (µM) of doxorubicin and palifosfamide were determined for each cell line grown as a monolayer and treated for 7 days. Values are expressed as mean and standard deviation (SD).

Three-dimensional cultures on collagen scaffolds

To compare the morphology of the primary culture with that of the patient's tissue, we seeded the cells on a 3D collagen-based scaffold, which provides a more faithful representation of cell population morphology than monolayer surfaces. Two million primary cells were seeded at the center of a collagen-based scaffold kindly provided by our collaborator Dr. Alessandro De Vita (IRCCS Istituto

Romagnolo per lo Studio dei Tumori (IRST) “Dino Amadori”). Cells were left to penetrate the scaffold in an incubator for at least 2 hrs. The cell-loaded scaffold was then filled with culture medium and kept in culture in an incubator for 7 days. At the end of the incubation, the scaffolds were formalin-fixed and embedded in paraffin. Our collaborator Dr. Giorgia Arcovito (Hospital Pathology Unit, IRCCS Ospedale Policlinico San Martino), analyzed the slides and found a general morphological resemblance to MFS. MFS001 consisted of discohesive cells characterized by abundant cytoplasm with intracytoplasmic mucin vacuoles; nuclei showed marked atypia, size variability, hyperchromasia, and prominent nucleoli. Overall, the cells were evaluated as neoplastic and mucin-producing. MFS002 consisted of cells that were partly discohesive and partly showed solid growth, with abundant cytoplasm containing intracytoplasmic mucin vacuoles. Marked nuclear atypia was also present, with the same features listed above. In addition, pleomorphic multinucleated elements were observed (typical of high-grade MFS). MFS003 showed disorganized solid growth; myxoid differentiation was barely recognizable or absent, and the appearance was more consistent with that of an UPS. The cells had abundant eosinophilic cytoplasm, spindle-to-epithelioid morphology, and highly atypical nuclei with the usual features (Figure 12).

MFS cells grown on collagen-based scaffolds showed morphological characteristics consistent with pathological analysis of original tumor specimens.

These results show that collagen-based scaffolds provide a more faithful representation of cell population morphology than monolayer surfaces, as the incorporation of extracellular matrix components better mimics tumor architecture, and open up new avenues for future preclinical studies aimed at investigating therapeutic responses in more physiologically relevant models.

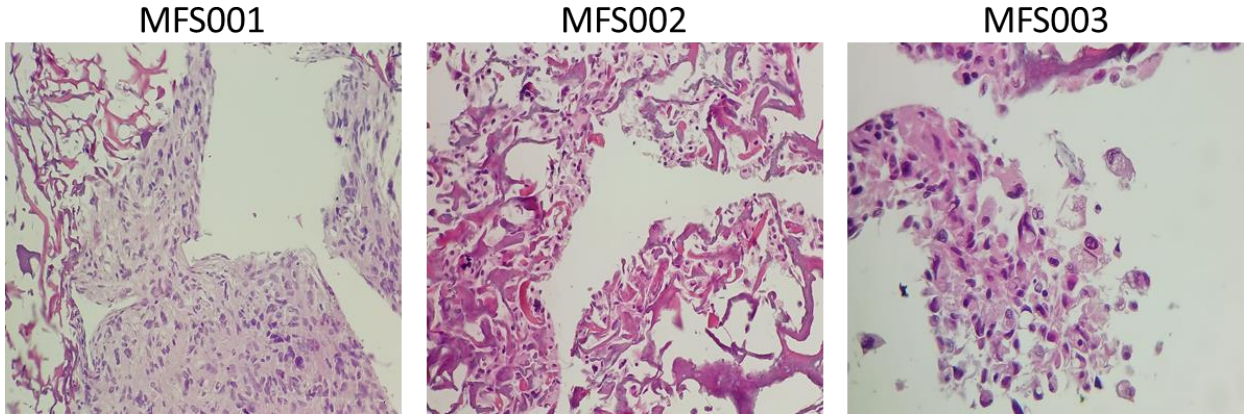

Figure 12: Hematoxylin and Eosin staining of MFS patient-derived primary culture. Some of the morphologic features of the tissue of origin are maintained, i.e., abundant cytoplasm with intracytoplasmic mucin vacuoles, and nuclear atypia (magnification 20x and 40x).

DISCUSSION

MFS exemplifies the intrinsic complexity of soft tissue sarcomas, combining marked biological heterogeneity, infiltrative growth, and limited therapeutic options. Despite its recognition as a distinct pathological entity, the clinical management of MFS continues to rely on treatment strategies developed for broader STS populations, reflecting the absence of validated histology-specific therapies [5]. While surgery with wide margins and radiotherapy remain the cornerstone of treatment for localized disease, systemic options for advanced or recurrent MFS are limited and only modestly effective. Anthracycline-based chemotherapy remains the standard of care, yet response rates are variable and frequently short-lived. This situation highlights a persistent and clinically relevant unmet need for improved biological understanding and for the development of more effective, personalized treatment strategies.

A major obstacle in MFS research is the scarcity of representative experimental models. The rarity of the disease, the advanced age of many patients, and the strong influence of the TME and ECM limit the availability and translational relevance of conventional in vitro systems. Increasing evidence suggests that traditional 2D cell culture models fail to capture essential features of sarcoma biology, including spatial organization, mechanical constraints, and complex cell–cell and cell–matrix interactions. In response to these limitations, recent international recommendations emphasize the importance of patient-derived three-dimensional (3D) sarcoma models as more faithful tools for biological investigation and therapeutic testing [9]. The present PhD project was therefore conceived to establish and characterize such models for MFS integrating molecular, immunological, and functional analyses. Although the patients' cohort analyzed in this study is numerically limited, its clinical characteristics are largely consistent with those reported in the literature. Patients were predominantly older adults, tumors most frequently arose in the extremities, and local recurrence represented a common clinical event [57]. These features align with classical clinicopathological descriptions of MFS and support the representativeness of the biological material used. Importantly, several samples were derived from relapsed or metastatic lesions, which may reflect more aggressive disease biology and therapy-resistant phenotypes.

Nevertheless, data from this small cohort should be interpreted as hypothesis-generating, providing a foundation for future investigations in larger, multicenter cohorts. The rarity of MFS and the practical challenges associated with fresh tissue collection underscore the importance of collaborative efforts and shared model platforms to advance the field.

A major finding of this study is the presence of a substantial immune infiltrate within MFS tumors, coupled with evidence of functional immune suppression. In previous reports, PD-L1 expression in MFS has been described in approximately 18% of cases, with considerable variability across cohorts and methodological approaches [21]. In our limited series, PD-L1 positivity by flow cytometry was

detected in two out of three primary cell lines, suggesting that immune checkpoint engagement may be more frequent in selected subsets of MFS than previously appreciated.

Multiparametric flow cytometry revealed that the MFS TME contains abundant $CD4^+$ and $CD8^+$ T lymphocytes, with a predominance of mature populations. Notably, both CD4+ and $CD8^+$ T cells largely displayed an effector memory phenotype, indicative of ongoing (or attempted) immune activation or responses against cancer, prior to antigen exposure. These findings argue against immune ignorance and instead suggest that MFS tumors are capable of eliciting an adaptive immune response. However, the high expression of inhibitory receptors such as PD-1, TIM-3, and LAG-3 on these T cells strongly indicates a state of functional exhaustion. The analysis of plasma biomarkers provided complementary insights into the systemic immune status of MFS patients. Elevated levels of interferon-γ (IFN-γ) were detected, consistent with ongoing immune activation. IFN-γ plays a central role in anti-tumor immunity by promoting antigen presentation and immune cell recruitment; however, chronic IFN-γ signaling can paradoxically contribute to immune dysfunction by inducing immune checkpoint expression and adaptive resistance mechanisms [35].

The presence of soluble immune checkpoint molecules in plasma further supports the concept of chronic immune activation accompanied by inhibitory feedback, a scenario that may ultimately result in immune exhaustion rather than tumor eradication. Together, tissue-based and systemic findings converge on a model in which MFS is characterized by an immune response that is initiated but not effectively executed, providing a strong rationale for therapeutic strategies aimed at reinvigorating exhausted immune cells.

T-cell exhaustion is a dynamic process driven by chronic antigen stimulation and sustained inflammatory signaling, resulting in impaired cytotoxic function and reduced proliferative capacity [22]. The co-expression of multiple inhibitory receptors observed in our samples is particularly relevant, as it has been associated with deeper exhaustion states and limited responsiveness to single-agent immune checkpoint blockade in other tumor types [49]. This observation raises important questions regarding the optimal immunotherapeutic strategy in MFS and suggests that combination approaches, targeting multiple inhibitory pathways or additional immunosuppressive mechanisms, may be required to restore effective anti-tumor immunity.

A critical prerequisite for successful T-cell–mediated tumor control is intact antigen presentation. In our models, HLA class I expression was consistently preserved, supporting the capacity of tumor cells to present antigens to $CD8^+$ T cells. This finding is particularly relevant given that loss of antigen presentation machinery represents a well-established mechanism of immune escape and resistance to immunotherapy [18]. The preservation of HLA class I, therefore, strengthens the biological rationale for immunotherapeutic interventions in MFS.

Another aspect that may interfere with immune cell-mediated tumor control is the presence of

immunosuppressive cell populations [53]. Indeed, our study shows that among $CD4^+$ T cells, a discrete proportion consists of Tregs endowed with immunosuppressive activity, which limits effective T-cell responses. Moreover, within the $CD45^+$ compartment, MDSCs and M2-polarized TAM are present, further inhibiting antitumor immunity. Altogether, our study demonstrates not only the presence of an exhausted T-cell compartment, but also an overall immunosuppressed TME. At the molecular level, MFS is defined by extensive genomic instability and frequent disruption of cell-cycle regulatory pathways. Among these, TP53 alterations represent one of the most recurrent and biologically significant events, with large sequencing studies reporting alterations in up to approximately half of MFS cases [80]. In line with these observations, TP53 alterations were identified in the majority of patient-derived models generated in this study, including both heterozygous and homozygous mutations.

Under normal conditions, p53 protein levels are tightly regulated and maintained at low levels through rapid degradation mediated primarily by the MDM2 ubiquitin–proteasome pathway [81]. Consequently, constitutive p53 accumulation, as observed in several of our models, is often indicative of missense TP53 mutations that stabilize the protein and may confer dominant-negative or gain-of-function properties [82]. The frequent detection of high basal levels of p21 further reflects dysregulation of cell-cycle checkpoints, although p21 expression alone cannot be interpreted as definitive evidence of intact p53 transcriptional activity due to its p53-independent regulation [83].

Functional assays following irradiation revealed substantial heterogeneity in p53 pathway activation across models. Interestingly, MFS003 cells, despite harboring a heterozygous TP53 mutation (R213Q), exhibited appreciable induction of p53 and p21 in response to DNA damage, suggesting partial preservation of p53 functionality. In contrast, the wild-type TP53 primary cell line MFS002 displayed weak induction and expressed a distinct p53 isoform, indicating non-canonical p53 regulation. These findings underscore the importance of functional characterization beyond mutational status, as different TP53 alterations can lead to diverse biological outcomes, including loss-of-function, dominant-negative effects, or oncogenic gain-of-function activities [82].

From a conceptual perspective, p53 dysfunction may contribute not only to uncontrolled proliferation but also to altered responses to stress, senescence, and immune modulation. Emerging evidence suggests that p53 can influence the composition and function of the TME, including immune cell recruitment and polarization [84]. Although these aspects were not directly addressed in the present study, they represent important avenues for future investigation.

The p53 pathway also plays a central role in mediating cellular responses to DNA-damaging agents such as doxorubicin and ifosfamide. Experimental studies have shown that restoration of wild-type p53 function can enhance sensitivity to anthracyclines in sarcoma models, whereas TP53 alterations may contribute to chemoresistance and poor clinical outcomes [40]. In our study, 2D drug testing

confirmed a degree of sensitivity of MFS models to doxorubicin and palifosfamide, supporting the intrinsic cytotoxic activity of these agents except for the MFS003 cells, harboring a heterozygous TP53 mutation, which proved to be more chemoresistant. However, it is increasingly recognized that 2D monolayer cultures provide an oversimplified representation of tumor biology and often fail to predict in vivo therapeutic responses. This limitation is particularly relevant for MFS, where tumor behavior is strongly influenced by ECM composition, mechanical properties, and spatial organization. These considerations highlight the need for more physiologically relevant models to accurately assess therapeutic efficacy.

To address these limitations, we implemented collagen-based 3D scaffold cultures, which allowed tumor cells to grow in a spatially organized environment more closely resembling native tissue architecture. Importantly, cells cultured in these scaffolds retained morphological features characteristic of their tumors of origin, as assessed by expert pathological evaluation. These findings are consistent with previous reports demonstrating that 3D sarcoma models better recapitulate in vivo morphology and treatment response than 2D systems [2,85].

Beyond morphological fidelity, scaffold-based models may offer a powerful platform to study tumor–ECM interactions, including invasion, matrix remodeling, and treatment-induced changes in ECM composition. These aspects are particularly relevant in MFS, which is defined histologically and biologically by its abundant myxoid matrix.

In conclusion, this PhD work addresses a significant gap in MFS research by establishing a comprehensive patient-derived preclinical platform that integrates tumor-intrinsic molecular features, immune contexture, and ECM architecture. The results demonstrate that MFS frequently exhibits an immune-infiltrated but functionally exhausted TME, preserved antigen presentation capacity, frequent yet heterogeneous TP53 alterations, and partial sensitivity to standard chemotherapeutic agents. Importantly, this work highlights the limitations of conventional 2D models and underscores the added value of 3D systems for studying MFS biology and therapeutic response.

Taken together, these findings provide a strong conceptual framework for future studies aimed at developing rational combination therapies targeting immune checkpoints, cell-cycle dysregulation, and the extracellular matrix. By leveraging clinically relevant 3D models, such approaches may ultimately contribute to improved, more personalized treatment strategies for patients with myxofibrosarcoma.

FUTURE PERSPECTIVES

Future studies will include an expanded collection of tumor samples to strengthen the robustness and representativeness of our results. In particular, we will further study TME exhaustion and immune suppression in order to find new actionable targets (either cellular or soluble) to be exploited in combination therapies for future clinical trials.

TP53's role in MFS deserves further investigations to demonstrate that TP53 alterations may contribute to chemoresistance and poor clinical outcomes and try to correlate it to immune suppression and exhaustion in TME. Moreover, the presence of a distinct p53 isoform different from the canonical 53-kDa protein warrants further studies to (i) evaluate the frequency of this finding and (ii) assess the functional impact of this isoform on p53 activity.

We provided proof of principle that collagen-based scaffolds are suitable for 3D culture and offer a more faithful representation of cell population morphology than monolayer surfaces, thereby opening new avenues for future preclinical studies aimed at investigating therapeutic responses in more physiologically relevant models. ECM-targeting strategies have not yet been systematically explored in MFS; we will cover this gap by investigating it in our preclinical models. Indeed, the 3D cultures developed in this project are particularly well suited to quantify ECM deposition, evaluate hyaluronan content, and test ECM-modulating approaches, alone or in combination with chemotherapy.

Finally, organotypic cultures generated from tumor fragments or cell suspensions derived from original tumor specimens will be pursued to evaluate different therapeutic approaches, including strategies aimed at enhancing immune cell infiltration and function while reducing immunosuppressive populations, potentially synergizing with immune checkpoint blockade.

REFERENCES

1. WHO Classification of Tumours Editorial Board. *Soft Tissue and Bone Tumours*. 5th ed. Lyon: IARC; 2020.
2. Stiller CA, Trama A, Serraino D, Rossi S, Navarro C, Chirlaque MD, et al. Descriptive epidemiology of sarcomas in Europe: report from the RARECARE project. *Eur J Cancer*. 2013;49(3):684–695.
3. Widemann BC, Italiano A. Biology and management of undifferentiated pleomorphic sarcoma, myxofibrosarcoma, and malignant peripheral nerve sheath tumors: state of the art and perspectives. *J Clin Oncol*. 2018;36(2):160–167.
4. Fletcher CDM, Bridge JA, Hogendoorn PCW, Mertens F, editors. *WHO Classification of Tumours of Soft Tissue and Bone*. 4th ed. Lyon: IARC; 2013.
5. Mentzel T, Calonje E, Wadden C, et al. Myxofibrosarcoma: clinicopathologic analysis of 75 cases. *Am J Surg Pathol*. 1996;20(4):391–405.
6. Kaya M, Wada T, Nagoya S, et al. MRI and histological evaluation of the infiltrative growth pattern of myxofibrosarcoma. *Skeletal Radiol*. 2008;37(12):1085–1090.
7. Lefkowitz RA, Landa J, Hwang S, et al. Myxofibrosarcoma: prevalence and diagnostic value of the “tail sign” on magnetic resonance imaging. *Skeletal Radiol*. 2013;42(6):809–818.
8. Lee J-C, Li C-F, Fang F-M, Wang J-W, Jeng Y-M, Yu SC, et al. Prognostic implication of MET overexpression in myxofibrosarcomas: an integrative array comparative genomic hybridization, real-time quantitative PCR, immunoblotting, and immunohistochemical analysis. Mod Pathol. 2010;23:1379–92.
9. Gronchi A, Miah AB, Dei Tos AP, et al. Soft tissue and visceral sarcomas: ESMO–EURACAN–GENTURIS Clinical Practice Guidelines. *Ann Oncol*. 2021;32(11):1348–1365.
10. Italiano A, Delva F, Mathoulin-Pélissier S, et al. Effect of surgery and radiotherapy on local control of myxofibrosarcoma. *Ann Surg Oncol*. 2010;17(11):2870–2875.
11. Pisters PWT, Leung DHY, Woodruff J, et al. Analysis of prognostic factors in 1,041 patients with localized soft tissue sarcomas of the extremities. *J Clin Oncol*. 1996;14(5):1679–1689.
12. Gronchi A, Lo Vullo S, Colombo C, et al. Extremity soft tissue sarcoma: local control directly impacts survival. *Ann Surg*. 2010;251(3):506–511.
13. Gronchi A, Colombo C, Fiore M, et al. Surgical margins and local recurrence in extremity soft tissue sarcoma: implications for survival. *Ann Surg*. 2010;251(3):506–511.
14. O’Sullivan B, Davis AM, Turcotte R, et al. Preoperative versus postoperative radiotherapy in soft-tissue sarcoma of the limbs: a randomised trial. *Lancet*. 2002;359(9325):2235–2241.

15. Colia V, Fiore M, Provenzano S, et al. Activity of anthracycline- and ifosfamide-based chemotherapy in patients affected by advanced myxofibrosarcoma. *Clin Sarcoma Res*. 2017;7:16.
16. Gronchi A, Palmerini E, Quagliuolo V, et al. Neoadjuvant chemotherapy in high-risk soft tissue sarcomas: final results of a randomized trial. *J Clin Oncol*. 2020;38(19):2178–2186.
17. Profumo C, Grassi M, Rigo V, et al. Unveiling the myxofibrosarcoma tumor microenvironment: implications for immunotherapy. *Front Immunol*. 2026;16:1717541.
18. Mowery YM, Ballman KV, Hong AM, et al. Pembrolizumab, radiation therapy, and surgery versus radiation therapy and surgery for stage III soft tissue sarcoma of the extremity: a randomized clinical trial. *Lancet*. 2024;404(10467):2053–2064.
19. Judson I, Verweij J, Gelderblom H, et al. Doxorubicin alone versus intensified doxorubicin plus ifosfamide for first-line treatment of advanced or metastatic soft-tissue sarcoma. *Lancet Oncol*. 2014;15(4):415–423.
20. van der Graaf WTA, Blay JY, Chawla SP, et al. Pazopanib for metastatic soft-tissue sarcoma (PALETTE). *Lancet*. 2012;379(9829):1879–1886.
21. Tawbi HA, Burgess M, Bolejack V, et al. Pembrolizumab in advanced soft-tissue sarcoma and bone sarcoma (SARC028). *Lancet Oncol*. 2017;18(11):1493–1501.
22. Keung EZ, Burgess M, Salazar R, et al. Correlative analyses of immune infiltration and response in the SARC028 trial. *Clin Cancer Res*. 2020;26(13):3339–3347.
23. Willems SM, Debiec-Rychter M, Szuhai K, Hogendoorn PCW, Sciot R. Local recurrence of myxofibrosarcoma is associated with increase in tumour grade and cytogenetic aberrations. Mod Pathol. 2006;19:407–16.
24. Idbaih A, Coindre J-M, Derré J, Mariani O, Terrier P, Ranchère D, et al. Myxoid malignant fibrous histiocytoma and pleomorphic liposarcoma share very similar genomic imbalances. Lab Invest. 2005;85:176–81.
25. Ohguri T, Hisaoka M, Kawauchi S, Sasaki K, Aoki T, Kanemitsu S, et al. Cytogenetic analysis of myxoid liposarcoma and myxofibrosarcoma by array-based CGH. J Clin Pathol. 2006;59:978–83.
26. Ma S, Fan L, Liu Y, Wang Y, Yu K, Wang L, et al. MET-overexpressing myxofibrosarcoma frequently exhibit polysomy of chromosome 7. Diagn Pathol. 2018;13:56.
27. Scheipl S, Brcic I, Moser T, Fischerauer S, Riedl J, Bergovec M, et al. Molecular profiling of soft-tissue sarcomas with FoundationOne® Heme. Ther Adv Med Oncol. 2021;13:17588359211029124.
28. Heitzer E, Sunitsch S, Gilg MM, Lohberger B, Rinner B, Kashofer K, et al. Expanded molecular profiling of myxofibrosarcoma. Mod Pathol. 2017;30:1698–709.

29. Ogura K, Hosoda F, Arai Y, Nakamura H, Hama N, Totoki Y, et al. Integrated genetic and epigenetic analysis of myxofibrosarcoma. Nat Commun. 2018;9:2765.
30. Takeuchi Y, Yoshida K, Halik A, Kunitz A, Suzuki H, Kakiuchi N, et al. The landscape of genetic aberrations in myxofibrosarcoma. Int J Cancer. 2022;151:565–77.
31. Laranga R, Pazzaglia L, Pedrini E, Sambri A, Ferrari C, Locatelli M, et al. p53 as a potential actionable target in myxofibrosarcoma. Lab Invest. 2024;104:102088.
32. Wang X, Yang J, Yang W, Sheng H, Jia B, Cheng P, et al. Multiple roles of p53 in cancer development. J Adv Res. 2025;75:539–60.
33. Zhao S, Wen H, Wang B, Xiong Q, Li L, Cheng A. p53: A player in the tumor microenvironment. Oncol Res. 2025;33:795–810.
34. Chen H, Song Y, Deng C, Xu Y, Xu H, Zhu X, et al. Immune infiltration and gene expression in sarcomas. Aging (Albany NY). 2020;13:2168–83.
35. Bisio A, Ciribilli Y, Fronza G, Inga A, Monti P. TP53 mutants in cancer progression. Hum Mutat. 2014;35:689–701.
36. Lin X, Wang L, Xie X, Qin Y, Xie Z, Ouyang M, et al. TP53 mutations and immunotherapy response in lung adenocarcinoma. Front Mol Biosci. 2020;7:602328.
37. Zhang Z, Hao R, Guo Q, Zhang S, Wang X. TP53 mutation and immune infiltration in breast cancer. Front Cell Dev Biol. 2021;9:759154.
38. Graadt van Roggen JF, Hogendoorn PCW, Fletcher CDM. Myxoid tumours of soft tissue. *Histopathology*. 2001;38(4):291–312.
39. Willems SM, Wiweger M, Graadt van Roggen JF, Hogendoorn PCW. Running GAGs: myxoid matrix in tumor pathology revisited. *Virchows Arch*. 2010;456:181–192.
40. Jacobetz MA, Chan DS, Neesse A, et al. Hyaluronan impairs vascular function and drug delivery in a mouse model of pancreatic cancer. Gut. 2013;62(1):112–120.
41. Morosi L, Meroni M, Ubezio P, et al. PEGylated recombinant human hyaluronidase (PEGPH20) pre-treatment improves intra-tumour distribution and efficacy of paclitaxel in preclinical models. J Exp Clin Cancer Res.2021;40:286.
42. Kouvidi K, Nikitovic D, Berdiaki A, Tzanakakis GN. Hyaluronan/RHAMM interactions in mesenchymal tumor pathogenesis. *Adv Cancer Res*. 2014;123:319–352.
43. Turley EA. Hyaluronan and cell locomotion. *Cancer Metastasis Rev*. 1992;11:21–30.
44. Sherman L, Sleeman J, Herrlich P, Ponta H. Hyaluronate receptors: key players in growth, differentiation, migration and tumor progression. *Curr Opin Cell Biol*. 1994;6:726–733.
45. Fernández-Tabanera E, Melero-Fernández de Mera RM, Alonso J. CD44 in sarcomas: a comprehensive review and future perspectives. *Front Oncol*. 2022;12:909450.

46. Hall CL, Turley EA. Hyaluronan: a ubiquitous glycosaminoglycan with multiple roles in tumor progression. *J Cell Biochem*. 1995;59:245–252.
47. Cox TR. The matrix in cancer. *Nat Rev Cancer*. 2021;21:217–238.
48. Nikitovic D, Kouvidi K, Berdiaki A, Karamanos NK, Tzanakakis GN. The role of hyaluronan in malignant progression. *Front Cell Dev Biol*. 2021;9:763640.
49. Genova C, Dellepiane C, Carrega P, Sommariva S, Ferlazzo G, Pronzato P, et al. Therapeutic implications of tumor microenvironment in lung cancer: focus on immune checkpoint blockade. *Front Immunol*. (2021) 12:799455. doi: 10.3389/fimmu.2021.799455
50. Zhao Z-Y, Chen Z-Y, Yu B, Xiao B, Liu L-Y, Xia Y, et al. Characterization of the immune cell infiltration landscape in myxofibrosarcoma to aid immunotherapy. *Front Immunol*. (2022) 13:916915. doi: 10.3389/fimmu.2022.916915
51. Palucka K, Banchereau J. Cancer immunotherapy via dendritic cells. Nat Rev Cancer. 2012 Mar 22;12(4):265-77. doi: 10.1038/nrc3258. PMID: 22437871; PMCID: PMC3433802.
52. Soilleux EJ, Rous B, Love K, Vowler S, Morris LS, Fisher C, et al. Myxofibrosarcomas contain large numbers of infiltrating immature dendritic cells. *Am J Clin Pathol*. (2003) 119:540–5. doi: 10.1309/JEB7-DGHH-01J1-1VUM
53. Tanaka A, Sakaguchi S. Regulatory T cells in cancer immunotherapy. Cell Res. 2017 Jan;27(1):109-118. doi: 10.1038/cr.2016.151. Epub 2016 Dec 20. PMID: 27995907; PMCID: PMC5223231.
54. Smolle MA, Herbsthofer L, Granegger B, Goda M, Brcic I, Bergovec M, et al. T-regulatory cells predict clinical outcome in soft tissue sarcoma patients: a clinico-pathological study. *Br J Cancer*. (2021) 125:717–24. doi: 10.1038/s41416-021-01456-0
55. Kim Y, Panda AK, and Shevach EM. Treg control of CD80/CD86 expression mediates immune system homeostasis. *Eur J Immunol*. (2025) 55:e202551771. doi: 10.1002/eji.202551771
56. Zong Y, Deng K, and Chong WP. Regulation of Treg cells by cytokine signaling and co-stimulatory molecules. *Front Immunol*. (2024) 15:1387975. doi: 10.3389/fimmu.2024.1387975
57. Yamashita A, Suehara Y, Hayashi T, Takagi T, Kubota D, Sasa K, et al. Molecular and clinicopathological analysis revealed an immuno-checkpoint inhibitor as a potential therapeutic target in a subset of high-grade myxofibrosarcoma. *Virchows Arch*. (2022) 481:1–17. doi: 10.1007/s00428-022-03358-9
58. Dancsok AR, Setsu N, Gao D, Blay J-Y, Thomas D, Maki RG, et al. Expression of lymphocyte immunoregulatory biomarkers in bone and soft-tissue sarcomas. *Modern Pathology*. (2019) 32:1772–85. doi: 10.1038/s41379-019-0312-y

59. Abeshouse A, Adebamowo C, Adebamowo SN, Akbani R, Akeredolu T, Ally A, et al. Comprehensive and integrated genomic characterization of adult soft tissue sarcomas. *Cell*. (2017) 171:950–965.e28. doi: 10.1016/j.cell.2017.10.014
60. Chen H, Liu H, Ai J, Du X, Sun Y, and Xiao S. PD1/PDL1 expression is associated with increased TIM3 expression and tumor-infiltrating T lymphocytes in fibroblastic tumors. *Clin Transl Oncol*. (2022) 24:586–96. doi: 10.1007/s12094-021-02723-5
61. Klaver Y, Rijnders M, Oostvogels A, Wijers R, Smid M, Grünhagen D, et al. Differential quantities of immune checkpoint-expressing CD8 T cells in soft tissue sarcoma subtypes. *J Immunother Cancer*. (2020) 8:e000271. doi: 10.1136/jitc-2019-000271
62. Luo Y, Min L, Zhou Y, Tang F, Lu M, Xie H, et al. Remarkable response to anti-PD1 immunotherapy in refractory metastatic high-grade myxofibrosarcoma patient. *Med (Baltimore)*. (2021) 100:e25262. doi: 10.1097/MD.0000000000025262
63. Song H-N, Kang MG, Park JR, Hwang J-Y, Kang JH, Lee WS, et al. Pembrolizumab for refractory metastatic myxofibrosarcoma: A case report. *Cancer Res Treat*. (2018) 50:1458–61. doi: 10.4143/crt.2017.529
64. Dancsok AR, Gao D, Lee AF, Steigen SE, Blay J-Y, Thomas DM, et al. Tumor-associated macrophages and macrophage-related immune checkpoint expression in sarcomas. *Oncoimmunology*. (2020) 9:1747340. doi: 10.1080/2162402X.2020.1747340 Baumgartner G, Gomar-Hössa C, Sakr L, Ulsperger E, Wogritsch C. The impact of extracellular matrix on the chemoresistance of solid tumors – experimental and clinical results of hyaluronidase as additive to cytostatic chemotherapy. Cancer Lett. 1998;131(1):85–99.
65. Jhunjhunwala S, Hammer C, Delamarre L. Antigen presentation in cancer: insights into tumour immunogenicity and immune evasion. Nat Rev Cancer. 2021 May;21(5):298-312. doi: 10.1038/s41568-021-00339-z. Epub 2021 Mar 9. PMID: 33750922.
66. Vargas AC, Maclean FM, Sioson L, Tran D, Bonar F, Mahar A, Cheah AL, Russell P, Grimison P, Richardson L, Gill AJ. Prevalence of PD-L1 expression in matched recurrent and/or metastatic sarcoma samples and in a range of selected sarcomas subtypes. PLoS One. 2020 Apr 15;15(4):e0222551. doi: 10.1371/journal.pone.0222551. PMID: 32294103; PMCID: PMC7159201.
67. Hu X, Garcia M, Weng L, Jung X, Murakami JL, Kumar B, Warden CD, Todorov I, Chen CC. Identification of a common mesenchymal stromal progenitor for the adult haematopoietic niche. Nat Commun. 2016 Oct 10;7:13095. doi: 10.1038/ncomms13095. PMID: 27721421; PMCID: PMC5062560.
68. Postiglione L, Di Domenico G, Caraglia M, Marra M, Giuberti G, Del Vecchio L, Montagnani S, Macri M, Bruno EM, Abbruzzese A, Rossi G. Differential expression and

cytoplasm/membrane distribution of endoglin (CD105) in human tumour cell lines: Implications in the modulation of cell proliferation. Int J Oncol. 2005 May;26(5):1193-201. doi: 10.3892/ijo.26.5.1193. PMID: 15809709.

69. Crane JN, Graham DS, Mona CE, Nelson SD, Samiei A, Dawson DW, Dry SM, Masri MG, Crompton JG, Benz MR, Czernin J, Eilber FC, Graeber TG, Calais J, Federman NC. Fibroblast Activation Protein Expression in Sarcomas. Sarcoma. 2023 Jun 9;2023:2480493. doi: 10.1155/2023/2480493. PMID: 37333052; PMCID: PMC10275689.
70. Mantovani A, Marchesi F, Malesci A, Laghi L, Allavena P. Tumour-associated macrophages as treatment targets in oncology. Nat Rev Clin Oncol. 2017 Jul;14(7):399-416. doi: 10.1038/nrclinonc.2016.217. Epub 2017 Jan 24. PMID: 28117416; PMCID: PMC5480600.
71. Gordon S, Taylor PR. Monocyte and macrophage heterogeneity. Nat Rev Immunol. 2005 Dec;5(12):953-64. doi: 10.1038/nri1733. PMID: 16322748.
72. Lasser SA, Ozbay Kurt FG, Arkhypov I, Utikal J, Umansky V. Myeloid-derived suppressor cells in cancer and cancer therapy. Nat Rev Clin Oncol. 2024 Feb;21(2):147-164. doi: 10.1038/s41571-023-00846-y. Epub 2024 Jan 8. PMID: 38191922.
73. Dunn GP, Koebel CM, Schreiber RD. Interferons, immunity and cancer immunoediting. Nat Rev Immunol. 2006 Nov;6(11):836-48. doi: 10.1038/nri1961. PMID: 17063185.
74. Hsieh HC, Ling LL, Wang YC. Post-translational modifications of immune checkpoints: molecular mechanisms, tumor microenvironment remodeling, and therapeutic implications. J Biomed Sci. 2026 Jan 4;33(1):3. doi: 10.1186/s12929-025-01202-1. PMID: 41486149; PMCID: PMC12765318.
75. Engeland K. Cell cycle regulation: p53-p21-RB signaling. Cell Death Differ. 2022 May;29(5):946-960. doi: 10.1038/s41418-022-00988-z. Epub 2022 Mar 31. PMID: 35361964; PMCID: PMC9090780.
76. Kubbutat MH, Jones SN, Vousden KH. Regulation of p53 stability by Mdm2. Nature. 1997 May 15;387(6630):299-303. doi: 10.1038/387299a0. PMID: 9153396.
77. Yue X, Zhao Y, Xu Y, Zheng M, Feng Z, Hu W. Mutant p53 in Cancer: Accumulation, Gain-of-Function, and Therapy. J Mol Biol. 2017 Jun 2;429(11):1595-1606. doi: 10.1016/j.jmb.2017.03.030. Epub 2017 Apr 6. PMID: 28390900; PMCID: PMC5663274.
78. Macleod KF, Sherry N, Hannon G, Beach D, Tokino T, Kinzler K, Vogelstein B, Jacks T. p53-dependent and independent expression of p21 during cell growth, differentiation, and DNA damage. Genes Dev. 1995 Apr 15;9(8):935-44. doi: 10.1101/gad.9.8.935. PMID: 7774811.
79. Waga S, Hannon GJ, Beach D, Stillman B. The p21 inhibitor of cyclin-dependent kinases controls DNA replication by interaction with PCNA. Nature. 1994 Jun 16;369(6481):574-8. doi: 10.1038/369574a0. PMID: 7911228.

80. Gartel AL, Radhakrishnan SK. Lost in transcription: p21 repression, mechanisms, and consequences. Cancer Res. 2005;65(10):3980–3985.
81. Olivier M, Hollstein M, Hainaut P. TP53 mutations in human cancers: origins, consequences, and clinical use. Cold Spring Harb Perspect Biol. 2010;2(1):a001008.
82. O'Connor PM, Jackman J, Bae I, Myers TG, Fan S, Mutoh M, et al. Characterization of the p53 tumor suppressor pathway in cell lines of the National Cancer Institute anticancer drug screen and correlations with the growth-inhibitory potency of 123 anticancer agents. Cancer Res. 1997;57(19):4285–4300.
83. De Cock L, Palubeckaite I, Bersani F, Faehling T, Pasquali S, Umbaugh S, et al. Establishment of patient-derived 3D in vitro models of sarcomas: literature review and guidelines on behalf of the FORTRESS working group. Neoplasia. 2025;65:101171.
84. Zhu KL, Su F, Yang JR, Xiao RW, Wu RY, Cao MY, Ling XL, Zhang T. TP53 to mediate immune escape in tumor microenvironment: an overview of the research progress. Mol Biol Rep. 2024 Jan 25;51(1):205. doi: 10.1007/s11033-023-09097-7. PMID: 38270700; PMCID: PMC10811008
85. Infante JR, Korn RL, Rosen LS, LoRusso P, Dychter SS, Zhu J, et al. Phase I trials of PEGylated recombinant human hyaluronidase PH20 in patients with advanced solid tumours. Br J Cancer. 2018;118(2):153–161.